

**ZFC Superconductor Magnetic Levitation System  
"Maglev-Tuga"**  
Guidance and Lateral Stability

**Francisco Ferreira da Silva**

Thesis to obtain the Master of Science Degree in  
**Electrical and Computer Engineering**

Supervisor: Prof. Paulo José da Costa Branco

**Examination Committee**

Chairperson: Prof. Rui Manuel Gameiro de Castro

Supervisor: Prof. Paulo José da Costa Branco

Member of the Committee: Prof. Vitor Manuel de Oliveira Maló Machado

**June 2018**



*To my Grandmother Alda, for the unconditional support.*





## **Declaration**

I declare that this document is an original work of my own authorship and that it fulfills all the requirements of the Code of Conduct and Good Practices of the Universidade de Lisboa



## **Acknowledgments**

First, I would like to say that it was a great pleasure to work under professor Paulo Branco, not only for his support, knowledge and advises given along the dissertation, but also for the friendship throughout the year. Second, I would like to thank my colleague António Costa, for the talks and the sharing of knowledge we had, as also for the help he gave me on the beginning of my experimental research for this dissertation. I also give thanks for the friendships I have made in the electrical machine laboratory, for the help and joy they gave me, making the workplace easier and fun for me.

To my best friends, that since the first year of college they are with me and helped me along the course, not only academically, but for the good times spent together.

To my parents, for being the first ones to push me to study and work hard, giving me the much needed education a guidance necessary to be here.

Last, but not least, to my grandmother Alda. Without you, this would have been a harder journey.



## Resumo

É feita a comparação entre duas geometrias para um veículo de levitação magnética usando supercondutores de alta temperatura (HTS), com zero-field-cooling (ZFC), do tipo YBCO. As duas geometrias são: uma geometria rectangular, que usa blocos de magnetos permanentes para fazer a pista magnética, e um carro com blocos supercondutores, que levitam sobre a pista magnética; uma nova geometria cilíndrica que consiste numa pista magnética cilíndrica discreta, feita de magnetos permanentes, igualmente espaçados, e de supercondutores com uma geometria de meio anel, a levitar na pista magnética, com um espaçamento radial constante. A métrica de comparação entre as duas geometrias é a estabilidade lateral.

Um protótipo já existente da geometria rectangular é usado para serem realizadas experiências para determinar a resposta do sistema a uma perturbação lateral. Para a nova geometria cilíndrica, simulações em 2D e 3D foram realizadas usando um programa de elementos finitos. As simulações serviram para o dimensionamento desta nova geometria, tendo em conta a grossura e profundidade dos supercondutores, do espaçamento entre os magnetos permanentes, e do espaçamento entre o superconductor e os magnetos. O dimensionamento teve em conta os supercondutores conseguirem estar em equilíbrio estático, i.e, a força de levitação estar equilibrada com a força gravítica do superconductor, tendo em vista manter a simetria do sistema. As duas geometrias foram comparadas em relação às suas respostas a perturbações laterais.

As conclusões chegadas foram que a geometria rectangular apresenta uma resposta não linear e os deslocamentos laterais máximos para o qual o sistema ainda é estável são por volta de 21 mm.

**Palavras-chave:** Superconductores de Alta Temperatura (HTS), Levitação Magnética (Maglev), Forças de Guiamento, Estabilidade Lateral



## Abstract

This dissertation makes the comparison between two types of geometries for a magnetic levitating vehicle using YBCO zero field cooled (ZFC) high temperature superconductors (HTS) under: a rectangular geometry, using rectangular bulks of permanent magnets to make the tracks, and a car with superconductors, levitating above the magnetic track; and a cylindrical geometry, consisting of a cylindrical magnetic track, with equally spaced permanent magnets, and superconductors with the geometry of an half ring, levitating on the cylindrical track, with a constant radial air gap. The metric for comparison is the lateral stability of both geometries.

The analysis made in this dissertation is the following: for the rectangular geometry, the prototype is used to make an analysis to estimate its response to lateral displacements. For the cylindrical geometry, 2D and 3D simulations are made using a finite element method (FEM) software. The simulations made are for the dimensioning of the new cylindrical geometry, regarding the thickness and depth of the YBCO superconductor half rings, the spacing between the permanent magnets, and the air gap between the YBCO superconductor half ring and the permanent magnets. These studies are evaluated and chosen considering if their levitating forces are close to the gravitational force of the superconductor, to maintain a constant radial air gap. The two geometries are then compared, regarding their response to lateral displacements.

It was found that, the rectangular geometry presents a non-linear response for a lateral displacement and the maximum displacement for which the system is still stable is around 21 mm. For the cylindrical geometry, the response is very close to linear and it has an inherent stability. However, the maximum displacements for the possible geometries can be lower than 21 mm, since the geometries that guarantee a stable levitation have a small air gap, and the air gap is closely related to the possible lateral movement, due to the nature of the geometry.

**Keywords:** High-temperature superconductor (HTS), Magnetic Levitation (Maglev), Guidance Forces, Lateral Stability





# Contents

Acknowledgments . . . . .	vii
Resumo . . . . .	ix
Abstract . . . . .	xi
List of Tables . . . . .	xvii
List of Figures . . . . .	xix
Nomenclature . . . . .	xxiii
<b>1 Introduction</b>	<b>1</b>
1.1 Motivation . . . . .	2
1.2 Topic Overview . . . . .	2
1.3 Objectives . . . . .	3
1.4 Thesis Outline . . . . .	3
<b>2 High Temperature Superconductors</b>	<b>5</b>
2.1 Fundamentals . . . . .	6
2.2 Critical Region and Superconductive States . . . . .	6
2.2.1 Diamagnetic State and Meissner Effect . . . . .	7
2.2.2 Mixed State and Flux Pinning . . . . .	8
2.3 Cooling Mechanisms . . . . .	9
2.3.1 Forces and Energy Losses in FC and ZFC Systems . . . . .	9
2.4 Electromagnetic Model Formulation . . . . .	11
2.4.1 HTS E-J Power Law . . . . .	11
2.4.2 Mathematical Description of the Magnetic Field $\mathbf{H}$ . . . . .	12
<b>3 Lateral Stability of the Rectangular Geometry Prototype</b>	<b>15</b>
3.1 System Description . . . . .	16
3.1.1 Description of the Lateral Movement . . . . .	17
3.1.2 System Lateral Dynamics . . . . .	17
3.2 Experimental Setup . . . . .	18
3.2.1 Force Field and Mass Measurement . . . . .	19
3.2.2 Transient Experiment . . . . .	20

<b>4</b>	<b>New HTS Cylindrical Geometry and Simulation Analysis</b>	<b>25</b>
4.1	Overview . . . . .	26
4.1.1	Geometric Description of the System . . . . .	26
4.2	Finite Element Method Model and Analysis . . . . .	27
4.2.1	H Formulation . . . . .	27
4.2.2	Maxwell Stress Tensor and Force Calculation . . . . .	28
4.2.3	Application Example of the Maxwell Stress Tensor . . . . .	31
4.3	Material Characteristics . . . . .	33
4.4	2D Distributed Parameters Model . . . . .	35
4.4.1	2D FEM Model . . . . .	35
4.4.2	Physical Interpretation of the 2D Simulation using FEM . . . . .	36
4.4.3	2D FEM Simulations for the Calculation of the Levitation Force $F_y$ . . . . .	37
4.4.4	Calculation of the Equilibrium Force $F_{Eq}$ . . . . .	39
4.5	Manufacturing and Budget Constraints: New Model and Second Simulation . . . . .	39
4.5.1	Piecewise HTS FEM Model . . . . .	39
4.5.2	2D FEM simulations of the New Piecewise HTS and Computation of the Levitation and Lateral Forces . . . . .	40
4.6	3D Distributed Parameter Model . . . . .	41
4.6.1	3D FEM Model . . . . .	41
4.6.2	3D FEM Simulations for the Calculation of the Levitation Force and Comparison with the 2D Results . . . . .	42
4.6.3	Liquid Nitrogen and YBCO Container Weight for the Computation of the Total Weight	43
4.6.4	3D FEM Simulations for the Computation of the Net Force Varying the YBCO Ge- ometric Parameters . . . . .	45
4.6.5	3D FEM Simulations for the Computation of the Net Force Varying the Permanent Magnets Spacing . . . . .	47
<b>5</b>	<b>Comparison of the Lateral Stability Between the Two Geometries</b>	<b>51</b>
5.1	Guidance Force of both geometries . . . . .	52
5.2	Lateral Response of both geometries . . . . .	53
5.2.1	Dynamic Equations and Comparison Model . . . . .	53
5.2.2	Results of the Comparison of the Dynamic Response of the Two Geometries . . .	54
<b>6</b>	<b>Conclusions</b>	<b>57</b>
6.1	Achievements . . . . .	58
6.2	Future Work . . . . .	58
	<b>Bibliography</b>	<b>59</b>
<b>A</b>	<b>Vector calculus</b>	<b>61</b>
A.1	Vector identities . . . . .	61

**B Technical Datasheets** **63**

B.1 UNAM 12U9914/S14 Ultrasonic Distance Measuring Sensor . . . . . 63

B.2 SCAIME K12 Force Sensor . . . . . 63



# List of Tables

4.1	Electromagnetic and mechanical parameters of the YBCO Bulk. . . . .	33
4.2	Electromagnetic and geometric parameters of the permanent magnets. . . . .	34
4.3	Values of the geometric variables for the parametric sweep. . . . .	37
4.4	Results for the air gap value for null resultant force, for each thickness, and the minimum of the fitting curve. . . . .	39
4.5	Values of the geometric variables used for the comparison between the 2D and 3D levitation forces. . . . .	43
4.6	Comparison between the values of the levitation forces in the 2D and 3D simulations. . .	43
4.7	Values of the geometric variables used for the computation of the YBCO levitation force $F_{lev3D}$ . . . . .	45
4.8	Levitation and net force values for the air gap values of 30 and 35 mm. . . . .	47
4.9	Values of the geometric variables used for the computation of the YBCO levitation force $F_{lev3D}$ . . . . .	48



# List of Figures

2.1	Volume defining the superconducting region [10]. . . . .	6
2.2	Possible superconductive states in an HTS. [11] . . . . .	7
2.3	Illustration of the <i>Meissner Effect</i> . The streamlines represent the magnetic field lines. Note that the superconductor repels the magnetic field. . . . .	7
2.4	SQUID microscopy scanning of the magnetic flux density tubes of a 200-nm-thick YBCO film [12]. . . . .	8
2.5	HTS subject to <i>flux pinning</i> [13]. In a diamagnetic state, the superconductor would normally expel the field, resulting in a higher downward force than the existing force of gravity of the HTS. Since the material is subject to <i>flux pinning</i> , the HTS is trapped in the magnetic field, resulting in a null net force. . . . .	8
2.6	HTS in a Field-Cooled process (a) and in a Zero-Field-Cooled process (b). In (a), the superconductor traps the magnetic field that penetrated him and can maintain that magnetic field, without an external source. in (b), the HTS repels the magnetic field that tries to penetrate. . . . .	9
2.7	Levitation forces obtained for the ZFC and FC system [1]. . . . .	10
2.8	(a) Guidance force versus ZFC system lateral displacement. (b) Guidance force versus FC system lateral displacement [1]. . . . .	10
2.9	Levitation forces obtained for the FC system with different cooling heights [1]. . . . .	10
3.1	Technical drawing of the HTS planar levitation prototype. . . . .	16
3.2	Depiction of the types of movements of the system. . . . .	16
3.3	Distribution of the magnetic flux density lines and resultant forces (adapted from [15]). In a), the car is center aligned with the magnetic track, resulting in a null net force. in b) and c) there is an attractive force to the center position when the magnetic track is displaced with respect to the YBCO car. . . . .	18
3.4	Experimental rig: a) Overall view of experimental rig b) Base of the experimental rig. c) Top view of magnetic rail. d) Top view of car which the four YBCO bulks are laid in. . . . .	19
3.5	Lateral forces with respect to the lateral displacement. . . . .	20
3.6	Overall view of experimental setup. . . . .	21

3.7	Oscillograms of the transient response to initial conditions with initial position (orange curves) of: a) 20 mm and b) 15 mm. The displacement reference is the center position. The blue curve is the trigger switch to pinpoint the start of the movement of the magnetic track. . . . .	21
3.8	Response of the system due to a initial condition of $x = 20 \text{ mm}$ and $x = 15 \text{ mm}$ . . . . .	22
3.9	root mean square error as a function of the friction coefficient $b$ . . . . .	22
3.10	Dynamic estimated for the $x_0 = 20 \text{ mm}$ response and the validation for the $x_0 = 15 \text{ mm}$ response. . . . .	23
4.1	Conceptual design of the magnetic rails of the new cylindrical geometry for the ZFC-Maglev vehicle. . . . .	26
4.2	New model of the ZFC-Maglev system: a) overall view of the model and b) front view of the model (2D Representation). . . . .	27
4.3	Example of cubic volume $V$ enclosed by the surface $S$ , displaying the top, bottom and right normal of the surface. . . . .	32
4.4	Example of cubic volume $V$ enclosed by the surface $S$ , displaying the tensors in each face. . . . .	33
4.5	Front view of YBCO half ring bulk with the magnetic rail. . . . .	34
4.6	Schematic of the cylindrical ZFC-Maglev geometric model used in the 2D electromagnetic simulations. . . . .	35
4.7	Initial conditions and representation of the magnetization direction in the PM used in the 2D simulations. . . . .	36
4.8	Results of the simulation. Here, the surface current density in the z component are shown in the color graph, and the black arrows are the magnetic vector field. . . . .	37
4.9	Levitation Force computed in the 2D simulations for different air gap and thickness values of the YBCO. . . . .	38
4.10	$F_y$ Data and the fitting curve. . . . .	38
4.11	Representation of the new geometry, satisfying the manufacturer constraints. . . . .	40
4.12	. . . . .	40
4.12	2D results of the Forces computed: a) Guidance Forces. b) Levitation Forces. . . . .	41
4.13	Schematic of the cylindrical ZFC-Maglev geometric model used in the 3D electromagnetic simulations. . . . .	42
4.14	Initial conditions and representation of the magnetization direction in the PM used in the 3D simulations. . . . .	42
4.15	Representation of the volumes in the YBCO container: a) volume of Liquid Nitrogen; b) container volume. . . . .	44
4.16	Weights of the YBCO, LN2 and the total weight for different air gaps and depths of the YBCO. . . . .	46
4.17	Net forces for a continuous magnetic track and for different air gaps and depths of the YBCO. . . . .	47



4.18	Depiction of the YBCO bulk centered with a PM of the magnetic track. . . . .	48
4.19	Net vertical forces for magnetic tracks with a PM spacing of 10 and 15 mm. . . . .	49
4.20	Levitation force deviations, in percentage, from the levitation forces of Section 4.6.4. . . . .	49
5.1	Lateral forces with respect to the lateral displacement of the rectangular and cylindrical geometries. . . . .	52
5.2	Undamped, Lateral response of the rectangular and cylindrical geometry for an initial displacement of $x_0 = 20$ mm, as well as the linear response, for comparison. . . . .	55
5.3	Undamped, Lateral response of the rectangular and cylindrical geometry for an initial displacement of $x_0 = 15$ mm, as well as the linear response, for comparison. . . . .	55



# Nomenclature

## Greek symbols

- $\mu$  Magnetic permeability.
- $\mu_r$  relative magnetic permeability.
- $\omega$  Angular frequency.
- $\rho$  Electric resistivity.
- $\rho_{YBCO}$  Mass density of YBCO.
- $\sigma$  Electric conductivity.

## Roman symbols

- B** Magnetic flux density vector.
- $B$  norm of the magnetic flux density.
- $b$  friction coefficient.
- $B_0$  Parameter of the equation describing the dependency  $J_c(B)$ .
- $B_{C1}$  Lower critical magnetic field density.
- $B_{C2}$  Higher critical magnetic field density.
- D** Displacement vector field.
- $D_{\mathbf{H}}$  Jacobian matrix of the magnetic field  $\mathbf{H}$ .
- $D_{\mathbf{J}}$  Jacobian matrix of the current density  $\mathbf{J}$ .
- $D_{PM}$  Diameter of the permanent magnets.
- $d_{PM}$  spacing distance between permanent magnets.
- E** Electric vector field.
- $E_0$  Parameter of E-J power-law.
- F** Force vector field.

$\mathbf{f}$	force density vector.
$F$	Norm of the force vector field.
$f$	norm of the force density vector.
$F_{lev2D}$	Levitation force of the 2D simulations.
$f_{lev2D}$	Levitation force density of the 2D simulations.
$F_{lev3D}$	Levitation force of the 2D simulations.
$g$	acceleration of gravity.
$\mathbf{H}$	Magnetic vector field.
$H_C$	Critical magnetic field.
$\mathbf{J}$	Current density vector.
$J$	norm of the current density vector.
$J_C$	Critical current density.
$J_{C0}$	Maximum critical current density (with no magnetic field applied).
$m$	mass.
$n$	Parameter of E-J power-law.
$R_{air}$	Radius of air gap between permanent magnets and YBCO.
RMSE	Root mean square error.
$T_C$	Critical temperature.
$U$	Voltage.
$V$	Volume.

### Subscripts

$Cyl$	Relative to the cylindrical geometry.
$g$	Relative to gravity.
$lat$	Relative to lateral.
$LN2$	Relative to liquid nitrogen.
$net$	Relative to a total quantity.
$PM$	Relative to the permanent magnets.
$Rect$	Relative to the rectangular geometry.

*YBCO* Relative to the YBCO.

*m, n* Tensor components

*mag* Relative to magnetic.

*max* Relative to maximum.

*x, y, z* Cartesian components.

### **Superscripts**

*Cyl* Relative to the cylindrical geometry.

*LN2* Relative to liquid nitrogen.

*Rect* Relative to the rectangular geometry.

*YBCO* Relative to the YBCO.

T Transpose.



# Chapter 1

## Introduction

This chapter describes the motivation and goals for this thesis. A topic overview of the use of superconductors in vehicle applications is also presented. To conclude, the objectives and thesis outline are stated.

## 1.1 Motivation

The studies presented in this dissertation are a continuity of previous research made, regarding the use of Zero Field Cooled (ZFC) High Temperature Superconductors (HTS) for the design of a new magnetic levitating system [1]. One main aspect was the comparison between field cooled (FC) and ZFC HTS. To prove such concept, the prototype of the rectangular geometry was developed, which is in Chapter 3, and studies regarding the levitating forces and lateral forces were made, as well as a study comparing the power losses of both cooling methods. The main conclusions of this research were that, although FC systems have a better stability than ZFC systems, their levitating forces are lower, and the guidance forces of FC systems are dependent on the initial cooling height. Lower levitating forces makes FC systems having more superconductors and magnets than ZFC systems, for the same application. This has implications on the costs between FC and ZFC systems, making FC systems more expensive. Regarding the guidance forces of FC systems, they are dependent on the initial cooling height, and are less strong for increased cooling heights, making the stability height dependent for FC systems, a situation that in ZFC systems does not happen. Also, the power losses are higher in FC systems, and can compromise their superconductivity state. One can conclude that ZFC systems present to be a better candidate for vehicle applications, since the objective for vehicles are to increase the efficiency, to achieve higher speeds and have the capability of higher loads. In this dissertation, all the studies will focus on vehicle applications using ZFC HTS, being a continuation of the previous work stated.

This dissertation follows a proposal of Bruno Painho's future work [2]. In [2], Painho briefly states about the stability and levitation forces of a new cylindrical geometry, and makes a positive remark of being more stable than the rectangular geometry.

## 1.2 Topic Overview

Nowadays there are several levitation systems being used, each using active elements, namely electromagnets. The Transrapid, of German design, with an experimental track in Germany and implemented in China, connecting Shanghai to its airport. In Japan, it is used the L0-Maglev, which is a high-speed maglev that is in developing and testing. In April 2015, it achieved the velocity record of 603 kilometers per hour for magnetic levitation systems [3]. For low speed applications, there is the Linimo maglev line, in Japan, which is an automated Urban Maglev system, with top speeds of 100 kilometers per hour and served more than 20 million passengers [4]. Recently, the Beijing municipal government has built China's second low-speed maglev line, S1 Line, which has a top speed of 105 kilometers per hour [5].

However, there has been a push for the development of a levitation based on passive elements, such as permanent magnets and superconductors. Brazil has developed a full scale magnetic levitating vehicle, using FC HTS, called the Maglev-Cobra. It was developed in Universidade Federal do Rio de Janeiro and a magnetic track was built, that connects two distant parts of the campus, and it is used as a method of transportation along the campus. It was designed to operate low speed, usually around 8 meters per second [6] [7].



## **1.3 Objectives**

The objectives of this thesis are: to study the lateral forces of the initial rectangular geometry prototype and to develop a model for the dynamics of the lateral movement; to make a new cylindrical geometry design of the superconductors and the permanent magnets regarding the levitation and guidance forces; to study and develop a model for the dynamics of the lateral movement of the new design; to compare both systems and discuss the outcomes.

## **1.4 Thesis Outline**

This thesis is divided in five chapters, being the first Chapter, this introductory one. Chapter 2 is dedicated to give some background about some aspects of the High Temperature Superconductors, and a more detailed specification about the differences of Zero-Field-Cooled and Field Cooled HTS. Chapter 3 describes the first prototype developed by Bruno Painho, and the experiments made to evaluate the responses to lateral disturbances. Chapter 4 presents the simulations done for the development of the new cylindrical geometry, regarding the levitation and guidance forces of the geometry. In Chapter 5, a collection of the main results of Chapter 3 and 4 is made, and a comparison between the models is made. Finally, Chapter 6 completes this work by presenting the main conclusions of this work.



## **Chapter 2**

# **High Temperature Superconductors**

This chapter provides a summary of high temperature superconductors characteristics, describing their behavior and unique phenomena.

## 2.1 Fundamentals

It is noted that some metals or oxide composites, when subjected to a low enough temperature, start to have negligible electrical resistance. Who first discovered this effect was Heike Kamerlingh Onnes [8], that used liquefied Helium (4.2 K) to cool down mercury and noticed that below a certain temperature, the resistance could not be measurable. This is called the superconductive state. Due to its low electrical resistance, a superconductor can carry high values of current without significant temperature increases and high joule losses, in comparison to normal conductors, such as copper, silver or gold. [8] Another consequence of the superconductive state is the perfect diamagnetism it possesses.

Later, it was discovered that some oxide composites, such as the  $L_aB_aC_uO$ , could be superconductive with temperatures as high as 35 K [9]. This results marked the first steps to the development of high temperature superconductors (HTS). Presently, the temperatures of superconductive state of some materials are around 100 K, such as the YBaCuO (YBCO) composite, used in this dissertation, and liquid Nitrogen can be used (boiling point of 77 K) instead of liquid Helium, to refrigerate.

The development of HTS induced new studies that confirmed that not all superconductors behave in the same matter, and type-I and type-II superconductors, respectively, were discovered. Type-I superconductors are the ones that need temperatures below 30 K to be superconductive. These usually are metals, present a perfect diamagnetism when near a magnetic field and are fully explained by the Bardeen–Cooper–Schrieffer (BCS) theory [8]. In this dissertation, type-I superconductors will not be further analyzed, and the main focus will be on type-II superconductors, also called high temperature superconductors, or HTS.

## 2.2 Critical Region and Superconductive States

Superconductivity is characterized by three parameters: the critical magnetic field  $H_C$ , the critical current density  $J_C$  and the critical temperature  $T_C$  [8]. If the material surpasses any of this values, it loses its superconductive state. Figure 2.1 shows the volume defining the superconductive region. Any of

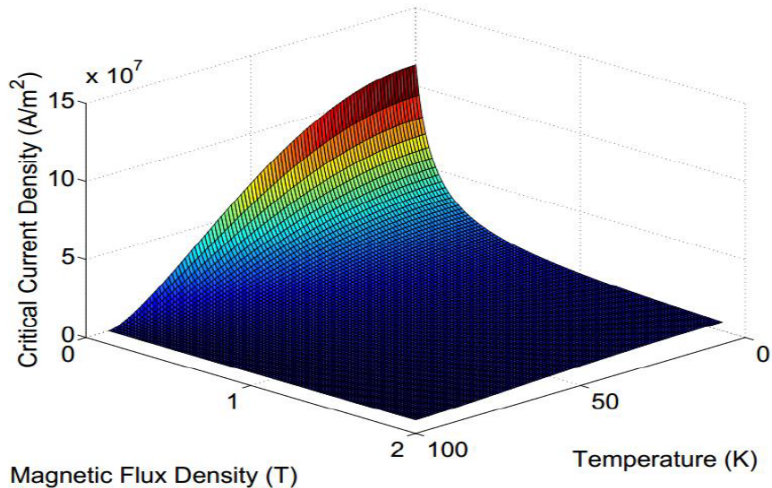


Figure 2.1: Volume defining the superconducting region [10].

these parameters can be exceeded only locally, turning some parts of the superconductor to a normal state. These parts will turn superconductive again once the quantities in question fall back below the respective critical values [10].

Regarding the magnetic field density in which the HTS is present, there can be two possible superconductive states, which are represented in Figure 2.2 . Those are the diamagnetic state and the mixed state.

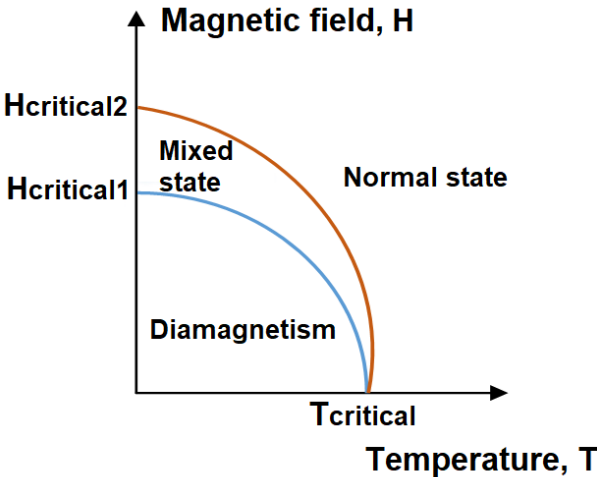


Figure 2.2: Possible superconductive states in an HTS. [11]

### 2.2.1 Diamagnetic State and Meissner Effect

Regarding Figure 2.2 , if the magnetic field density  $B$  is lower than  $B_{C1}$ , the superconductor is in its diamagnetic state, and the superconductor repels the magnetic field that tries to penetrate it. This effect is called the *Meissner Effect* [8] [9] [10] and it is represented in Figure 2.3.

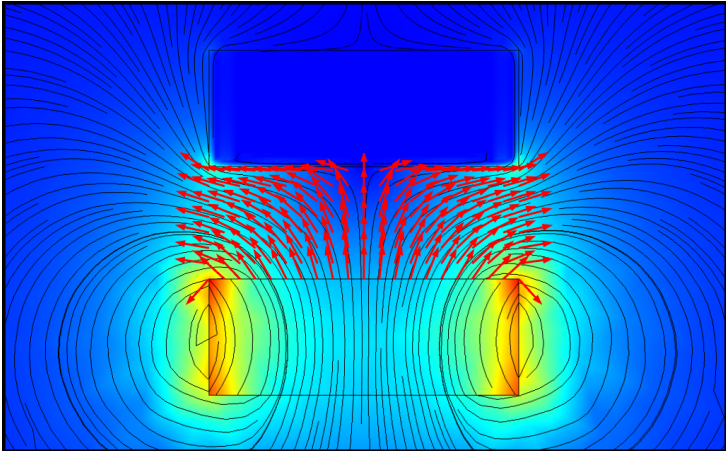


Figure 2.3: Illustration of the *Meissner Effect*. The streamlines represent the magnetic field lines. Note that the superconductor repels the magnetic field.

## 2.2.2 Mixed State and Flux Pinning

If the field is between  $B_{C1}$  and  $B_{C2}$ , with  $B_{C1} < B_{C2}$ , the superconductor loses its property of magnetic field expulsion and enters the mixed state. In this mixed state, the magnetic field lines penetrate the superconductor in non superconductive regions, where impurities exist, and microscopic tubes are created, allowing the concentration of a magnetic flux. This causes an electric current to flow, and surrounds those tubes of magnetic flux, creating what is called as Abrikosov vortices. Figure 2.4 shows the tubes of magnet flux in an YBCO sample.

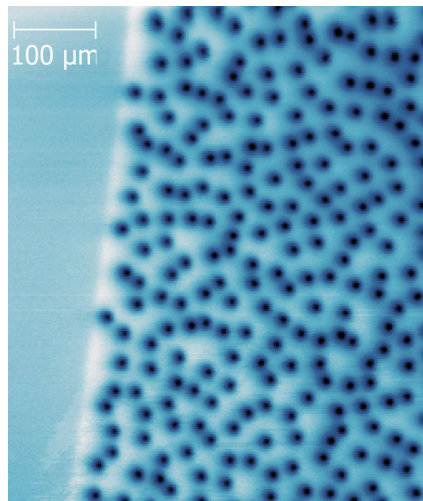


Figure 2.4: SQUID microscopy scanning of the magnetic flux density tubes of a 200-nm-thick YBCO film [12].

Due to the vortices, in this mixed state, a magnetic field can be trapped inside the superconductor, making the superconductor being in a region of space where the net force is null. This effect is called *flux pinning*, represented in Figure 2.5.

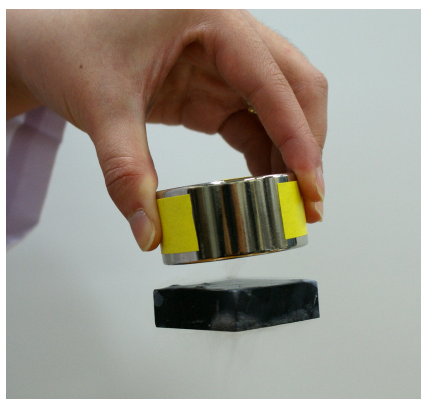


Figure 2.5: HTS subject to *flux pinning* [13]. In a diamagnetic state, the superconductor would normally expel the field, resulting in a higher downward force than the existing force of gravity of the HTS. Since the material is subject to *flux pinning*, the HTS is trapped in the magnetic field, resulting in a null net force.

### 2.3 Cooling Mechanisms

When a HTS is cooled under the presence of a magnetic field, it retains that magnetic field when it reaches its superconductive state. This cooling mechanism is called *Field-Cooling* (FC) and it is represented in Figure 2.6a. When field-cooled, if the superconductor is again exposed to an external magnetic field, it will try to align its internal field to the external field, making the superconductor trapped in that stable position, as it is in Figure 2.5.

If the superconductor is cooled without the presence of a magnetic field, it will try to retain that configuration, which means that any external field that tries to penetrate the superconductor will be repelled. This method of cooling is called Zero-Field-Cooling (ZFC). Both FC and ZFC are represented in Figure 2.6.

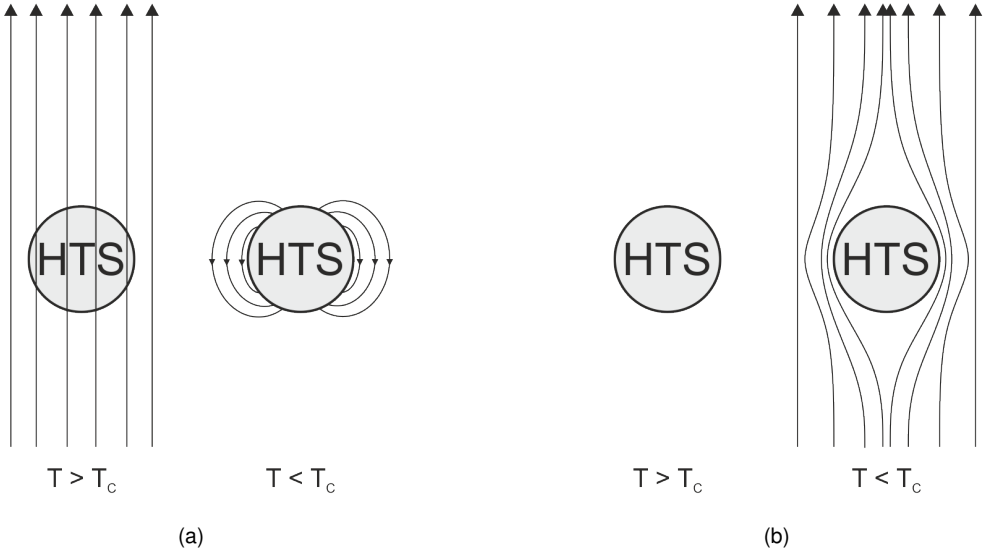


Figure 2.6: HTS in a Field-Cooled process (a) and in a Zero-Field-Cooled process (b). In (a), the superconductor traps the magnetic field that penetrated him and can maintain that magnetic field, without an external source. in (b), the HTS repels the magnetic field that tries to penetrate.

#### 2.3.1 Forces and Energy Losses in FC and ZFC Systems

In [1], a comparison between the vertical and horizontal forces of a superconductor maglev system using ZFC and FC HTS is made. Figure 2.7 shows the levitation forces for the ZFC and FC system. The conclusions of the experiment are that the ZFC system has higher levitation forces. This guarantees that the ZFC system can support more weight than the FC system.

Regarding the lateral stability, Figure 2.8 shows the horizontal forces with respect to a lateral displacement in a ZFC and FC system. This figure shows that the FC system has a better stability than ZFC systems, since their horizontal forces are higher. However, the FC system has a drawback: their joule losses are higher than the ZFC system. Since the horizontal forces are higher and the force is  $F = B \times J$ , this means that higher forces in a constant magnetic field density produce a higher current density inside the superconductor, which produce higher joule losses.

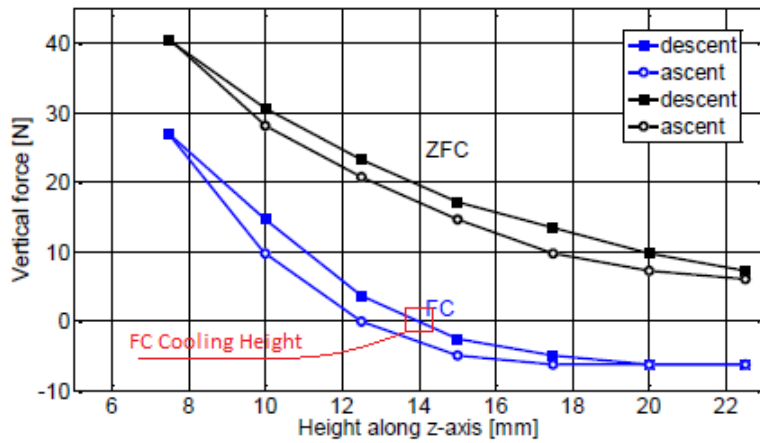


Figure 2.7: Levitation forces obtained for the ZFC and FC system [1].

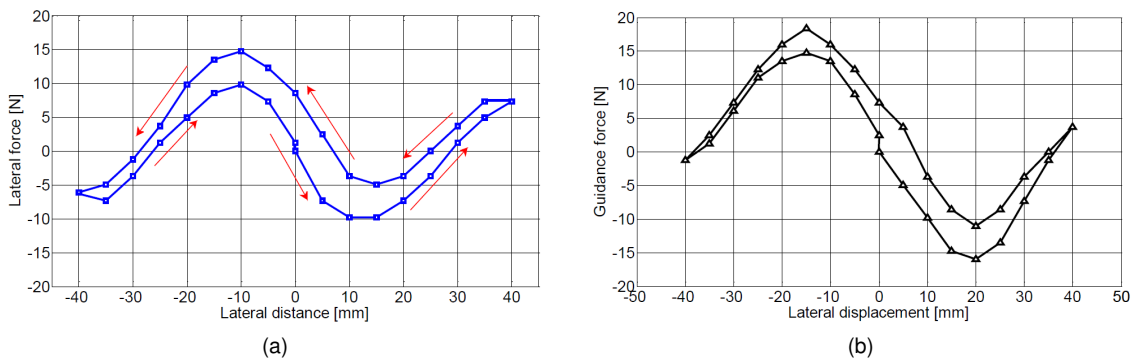


Figure 2.8: (a) Guidance force versus ZFC system lateral displacement. (b) Guidance force versus FC system lateral displacement [1].

The horizontal forces in the FC system are dependent on the initial cooling height, and are less strong for increased cooling heights. Figure 2.9 shows the dependency of the horizontal forces with respect to the cooling height. With this results, it is shown that the stability of the FC system varies with the cooling height, making this system more complex than the ZFC system.

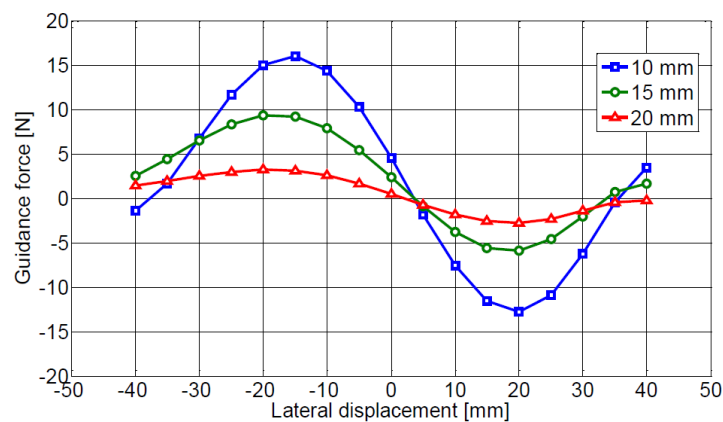


Figure 2.9: Levitation forces obtained for the FC system with different cooling heights [1].

It is with these results of [1] that the ZFC HTS system was preferred over the FC HTS system, for vehicle applications.



## 2.4 Electromagnetic Model Formulation

The foundations for this model stand on the Maxwell's equations in a quasi-stationary regime, neglecting the displacement vector  $\mathbf{D}$ , since the capacitive effects are negligible. For this type of regime, one has

$$\nabla \times \mathbf{E} = -\frac{\partial \mathbf{B}}{\partial t} \quad (2.1a)$$

$$\nabla \cdot \mathbf{B} = 0 \quad (2.1b)$$

$$\nabla \times \mathbf{H} \approx \mathbf{J} \quad (2.1c)$$

where  $\mathbf{E}$  is the electric field vector,  $\mathbf{B}$  is the magnetic flux density vector,  $\mathbf{H}$  is the magnetic field vector and  $\mathbf{J}$  is the current density vector. To completely solve Maxwell's equations, one needs relations between  $\mathbf{B}$  and  $\mathbf{H}$ , and between  $\mathbf{E}$  and  $\mathbf{J}$ . These are the constitutive relations, and for the magnetic fields, it is used the relation for isotropic linear materials and media

$$\mathbf{B} = \mu \mathbf{H}. \quad (2.2)$$

where  $\mu$  is the magnetic permeability.

### 2.4.1 HTS E-J Power Law

For type II superconductors, there is a non linear constitutive relation between the electric field  $\mathbf{E}$  and the current density  $\mathbf{J}$ , for low current densities (below or near the maximum critical current density  $J_{C0}$ ) [14]

$$\mathbf{E} = E_0 \left( \frac{J}{J_C} \right)^n \frac{\mathbf{J}}{J}, \quad (2.3)$$

where  $E_0$  and  $n$  are parameters that depend on the superconductor, and  $J_C$  is the critical current density, which depends on the magnetic flux density

$$J_C = \frac{B_0}{B_0 + B} J_{C0}. \quad (2.4)$$

The term  $J_{C0}$  in (2.4) represents the maximum critical current density of the material (for  $B = 0$ ). This value is temperature dependent, while  $B_0$  represents the value of the applied magnetic flux density that reduces the value of the critical current density to half of its maximum value  $J_C(B_0) = J_{C0}/2$ .

With (2.3) and (2.4) and wanting to make a relationship with the linear constitutive relation  $\mathbf{E} = \rho \mathbf{J}$ , one has the value of the resistivity:

$$\rho = \frac{E_0}{J_{C0}} \left( \frac{B_0 + B}{B_0} \right)^n \left( \frac{J}{J_{C0}} \right)^{n-1}. \quad (2.5)$$

## 2.4.2 Mathematical Description of the Magnetic Field $\mathbf{H}$

Using Faraday's law (2.1a), Ampere's law (2.1c), the magnetic constitutive relation (2.2) and (2.3) with (2.5)

$$\begin{cases} \nabla \times \mathbf{E} = -\mu \frac{\partial \mathbf{H}}{\partial t} \\ \nabla \times \mathbf{H} = \mathbf{J} \\ \mathbf{E} = \frac{E_0}{J_{C0}} \left( \frac{B_0 + \mu H}{B_0} \right)^n \left( \frac{J}{J_{C0}} \right)^{n-1} \mathbf{J} \end{cases}, \quad (2.6)$$

one has

$$\nabla \times \left( \frac{E_0}{J_{C0}} \left( \frac{B_0 + \mu H}{B_0} \right)^n \left( \frac{|\nabla \times \mathbf{H}|}{J_{C0}} \right)^{n-1} \nabla \times \mathbf{H} \right) = -\mu \frac{\partial \mathbf{H}}{\partial t}. \quad (2.7)$$

Equation (2.7) is a non linear partial differential equation with respect to space and time. This equation is solved using a FEM software, and the solved magnetic field  $\mathbf{H}$  can be used to calculate the magnetic flux density  $\mathbf{B}$  and the current density  $\mathbf{J}$ , using (??) and (2.1c), respectively. Nonetheless, this equation can be further analyzed, to get some information of the characteristics of the magnetic field near the HTS.

Using (2.7) without describing the  $\rho$  parameter

$$\nabla \times (\rho (\nabla \times \mathbf{H})) = -\mu \frac{\partial \mathbf{H}}{\partial t}, \quad (2.8)$$

and using the vector identity for  $\nabla \times (\rho (\nabla \times \mathbf{H}))$ <sup>1</sup>

$$\nabla \rho \times (\nabla \times \mathbf{H}) + \rho (\nabla \times (\nabla \times \mathbf{H})) = -\mu \frac{\partial \mathbf{H}}{\partial t}. \quad (2.9)$$

The second term of the right-hand side also has a vector identity associated with it

$$\nabla \times (\nabla \times \mathbf{H}) = \nabla (\nabla \cdot \mathbf{H}) - (\nabla \cdot \nabla) \mathbf{H}, \quad (2.10)$$

where  $\nabla \cdot \nabla$  is the vector Laplacian and it has the form of

$$\nabla \cdot \nabla = \nabla^2 = \frac{\partial^2}{\partial x^2} + \frac{\partial^2}{\partial y^2} + \frac{\partial^2}{\partial z^2}. \quad (2.11)$$

The vector Laplacian is the application of the scalar Laplacian to each of the components of the vector. In this case

$$\nabla^2 \mathbf{H} = \begin{bmatrix} \frac{\partial^2 H_1}{\partial x^2} + \frac{\partial^2 H_1}{\partial y^2} + \frac{\partial^2 H_1}{\partial z^2} \\ \frac{\partial^2 H_2}{\partial x^2} + \frac{\partial^2 H_2}{\partial y^2} + \frac{\partial^2 H_2}{\partial z^2} \\ \frac{\partial^2 H_3}{\partial x^2} + \frac{\partial^2 H_3}{\partial y^2} + \frac{\partial^2 H_3}{\partial z^2} \end{bmatrix}. \quad (2.12)$$

With (2.10) and knowing that  $\nabla \cdot \mathbf{H} = 0$ , (2.9) becomes

$$\nabla^2 \mathbf{H} = \frac{\nabla \rho}{\rho} \times (\nabla \times \mathbf{H}) + \frac{\mu}{\rho} \frac{\partial \mathbf{H}}{\partial t}. \quad (2.13)$$

---

<sup>1</sup>  $\nabla \times (\rho \mathbf{A}) = \nabla \rho \times \mathbf{A} + \rho (\nabla \times \mathbf{A})$

Equation (2.13) describes the magnetic field. By knowing the Laplacian of the magnetic field, one can describe the entire field. However, the Laplacian of the magnetic field is a function of the changes in space and time of the magnetic field, which makes the solution of this equation to be dependent on time initial conditions and boundary conditions. To add to the complexity, it has the gradient of the resistivity, which itself is a function of  $\mathbf{H}$ . Note that (2.5) can be described only using  $\mathbf{H}$  (which is in (2.7), but it is mentioned here again, for clarity)

$$\rho = \frac{E_0}{J_{C0}} \left( \frac{B_0 + \mu H}{B_0} \right)^n \left( \frac{\|\nabla \times \mathbf{H}\|}{J_{C0}} \right)^{n-1}, \quad (2.14)$$

which means that  $\nabla^2 \mathbf{H}$  is not described by external quantities, but entirely by itself, and the current is not imposed, but a consequence of the magnetic field imposed, external to the HTS.

Looking at (2.13), and assuming  $\mathbf{H}$  does not change over time, a steady-state solution can be achieved

$$\nabla^2 \mathbf{H} = \frac{\nabla \rho}{\rho} \times (\nabla \times \mathbf{H}), \quad (2.15)$$

if the right-hand side term is not null. To know if that is the case,  $\nabla \rho$  needs to be known. Since  $\nabla \times \mathbf{H} = \mathbf{J}$ , the mathematical analysis will use  $\mathbf{J}$  for simplification.

Using (2.14) and rearranging it to

$$\rho = \frac{E_0}{(J_{C0} B_0)^n} (B_0 + \mu H)^n J^{n-1}, \quad (2.16)$$

the partial derivative with respect to a space coordinate  $x_i$  is

$$\frac{\partial \rho}{\partial x_i} = \frac{E_0}{(J_{C0} B_0)^n} \left( n (B_0 + \mu H)^{n-1} \mu \frac{\partial H}{\partial x_i} J^{n-1} + (n-1) (B_0 + \mu H)^n J^{n-2} \frac{\partial J}{\partial x_i} \right), \quad (2.17)$$

which can be further simplified, taking the term  $(B_0 + \mu H)^n J^{n-1}$  out of the parenthesis, into

$$\frac{\partial \rho}{\partial x_i} = \rho \left( \mu \frac{n}{B_0 + \mu H} \frac{\partial H}{\partial x_i} + \frac{n-1}{J} \frac{\partial J}{\partial x_i} \right). \quad (2.18)$$

The gradient of the resistivity,  $\nabla \rho$ , is described as <sup>2</sup>

$$\nabla \rho = \begin{bmatrix} \frac{\partial \rho}{\partial x} \\ \frac{\partial \rho}{\partial y} \\ \frac{\partial \rho}{\partial z} \end{bmatrix}, \quad (2.19)$$

and using (2.18),  $\nabla \rho$  is

$$\nabla \rho = \rho \left( \mu \frac{n}{B_0 + \mu H} \nabla H + \frac{n-1}{J} \nabla J \right). \quad (2.20)$$

With (2.20), one can rewrite (2.15) as

$$\nabla^2 \mathbf{H} = \mu \frac{n}{B_0 + \mu H} (\nabla H \times \mathbf{J}) + \frac{n-1}{J} (\nabla J \times \mathbf{J}). \quad (2.21)$$

---

<sup>2</sup>any gradient of a scalar field  $\phi$  can be described as a column vector  $\nabla \phi = \left( \frac{\partial \phi}{\partial x}, \frac{\partial \phi}{\partial y}, \frac{\partial \phi}{\partial z} \right)$ .

All is left to know are the gradients of the norms of the magnetic field and the current density,  $H$  and  $J$ , respectively. To do this, note that

$$\frac{\partial}{\partial x_i} (H^2) = \frac{\partial}{\partial x_i} (\mathbf{H} \cdot \mathbf{H}) = \frac{\partial \mathbf{H}}{\partial x_i} \cdot \mathbf{H} + \mathbf{H} \cdot \frac{\partial \mathbf{H}}{\partial x_i} = 2 \left( \mathbf{H} \cdot \frac{\partial \mathbf{H}}{\partial x_i} \right), \quad (2.22)$$

and for the derivative of the norm, the chain rule is applied to (2.22) to give

$$\frac{\partial}{\partial x_i} (H) = \frac{\partial}{\partial x_i} \left( \sqrt{\mathbf{H} \cdot \mathbf{H}} \right) = \frac{\mathbf{H}}{\sqrt{\mathbf{H} \cdot \mathbf{H}}} \cdot \frac{\partial \mathbf{H}}{\partial x_i} = \frac{\mathbf{H}}{H} \cdot \frac{\partial \mathbf{H}}{\partial x_i}. \quad (2.23)$$

The gradient of the norm is, then

$$\nabla H = \frac{1}{H} \begin{bmatrix} \mathbf{H} \cdot \frac{\partial \mathbf{H}}{\partial x} \\ \mathbf{H} \cdot \frac{\partial \mathbf{H}}{\partial y} \\ \mathbf{H} \cdot \frac{\partial \mathbf{H}}{\partial z} \end{bmatrix}. \quad (2.24)$$

In (2.24),  $\nabla H$  can be described in another way. Considering that the derivative of  $\mathbf{H}$  with respect to a coordinate is still a column vector, then  $\nabla H$  can be described as

$$\nabla H = \frac{1}{H} \begin{bmatrix} \frac{\partial H_1}{\partial x} & \frac{\partial H_2}{\partial x} & \frac{\partial H_3}{\partial x} \\ \frac{\partial H_1}{\partial y} & \frac{\partial H_2}{\partial y} & \frac{\partial H_3}{\partial y} \\ \frac{\partial H_1}{\partial z} & \frac{\partial H_2}{\partial z} & \frac{\partial H_3}{\partial z} \end{bmatrix} \begin{bmatrix} H_1 \\ H_2 \\ H_3 \end{bmatrix} = \frac{1}{H} D_{\mathbf{H}}^T \mathbf{H}, \quad (2.25)$$

where  $D_{\mathbf{H}}$  is the jacobian matrix of the vector field.<sup>3</sup> For clarification, in (2.25), the superscript T in  $D_{\mathbf{H}}$  is to indicate the transpose of the matrix. Combining the vector  $\mathbf{H}$  with its norm in (2.25), one gets the unit vector of  $\mathbf{u}_{\mathbf{H}}$ , and  $\nabla H$  is a directional derivative of  $\mathbf{H}$  in the directional  $\mathbf{u}_{\mathbf{H}}$ <sup>4</sup>

$$\nabla H = D_{\mathbf{H}}^T \mathbf{u}_{\mathbf{H}}. \quad (2.26)$$

In the same manner,  $\nabla J$  can be described in the same way as  $\nabla H$

$$\nabla J = D_{\mathbf{J}}^T \mathbf{u}_{\mathbf{J}}. \quad (2.27)$$

So, (2.21) becomes

$$\nabla^2 \mathbf{H} = \mu \frac{n}{B_0 + \mu H} \left( (D_{\mathbf{H}}^T \mathbf{u}_{\mathbf{H}}) \times \mathbf{J} \right) + \frac{n-1}{J} \left( (D_{\mathbf{J}}^T \mathbf{u}_{\mathbf{J}}) \times \mathbf{J} \right). \quad (2.28)$$

Note that the right-hand side of (2.28) does not have a particularity that makes it a null result. This strongly indicates that in a general way the superconductor reaches a steady-state condition, where the magnetic field does not change in time.

<sup>3</sup> $D_{\mathbf{H}}$  can also be written as  $\nabla \mathbf{H}$ .

<sup>4</sup> $D_{\mathbf{H}}^T \mathbf{u}_{\mathbf{H}}$  is also written as  $(\mathbf{u}_{\mathbf{H}} \cdot \nabla) \mathbf{H}$ , an expression generally used in continuum mechanics.

## **Chapter 3**

# **Lateral Stability of the Rectangular Geometry Prototype**

This chapter describes the existing prototype, of rectangular geometry, and presents a transient and steady state response analysis regarding the lateral stability.

### 3.1 System Description

The rectangular geometry prototype is shown in Figure 3.1. It is composed by two separated parts: i) one fixed part containing an array of 2x2 superconductor bulks and ii) one movable part formed by an array of 3x4 neodymium permanent magnets. The middle row of magnets is shifted and with an opposite magnetic polarization from the two other rows, as it is shown in Figure 3.1,

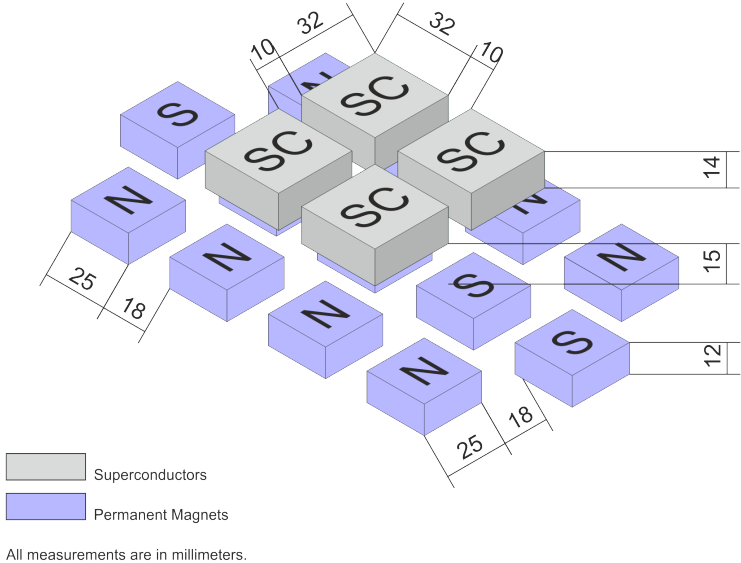


Figure 3.1: Technical drawing of the HTS planar levitation prototype.

Figure 3.2 depicts the movements the system may experience in this study. This thesis will only focus on the lateral stability and guidance forces, being disregarded the forward motion.

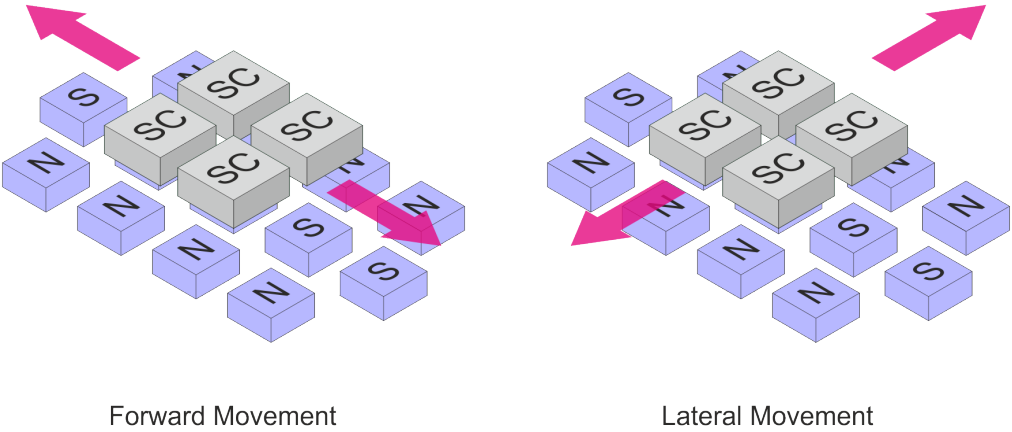


Figure 3.2: Depiction of the types of movements of the system.

### 3.1.1 Description of the Lateral Movement

Regarding the lateral movement, there is a stable position for the superconductors to be with respect to the magnetic track. When the middle line of the rows of the superconductors are aligned with the middle line of the gaps between the rows of permanent magnets, the resultant lateral magnetic force is null, and the superconductors are laterally stable [15]. To see this better, Figure 3.3 shows the magnetic flux density distribution when the car is center aligned with the magnetic track, which is its stable position (Figure 3.3a) and when it is off-centered to the left or to the right (Figure 3.3b and 3.3c, respectively). When the HTS car is center aligned with the magnetic track, the resultant force is null, and the car is in a stable position. When they are off center, the net force will not be null, and it will have the opposite direction of the direction of the movement. This means that there will be an attractive force to the center position if they are laterally displaced. This attraction force will occur if the displacements are no further than 21.5 mm from the center position [15]. If the displacement is higher, the forces will be in the direction of the movement, making the system unstable.

### 3.1.2 System Lateral Dynamics

Since the system has an attractive force towards the center, one can make a relationship between the magnetic force  $F$  and the displacement from the center  $x$ :

$$\begin{cases} F_{mag} > 0 & , x < 0 \\ F_{mag} = 0 & , x = 0 \\ F_{mag} < 0 & , x > 0 \end{cases} \quad (3.1)$$

This relationship expresses that the force is symmetric to the displacement

$$F_{mag} = -f(x), \quad (3.2)$$

being  $f(x)$  a function with respect to the displacement. With (3.2), and considering that the aerodynamic friction force is proportional to the velocity, one can express the system's dynamic as:

$$m\ddot{x} + b\dot{x} + f(x) = 0. \quad (3.3)$$

Equation (3.3) is the one used to estimate the lateral dynamics of the system using the experimental data. In Section 3.2.2, it is covered the experiments made to have the system's response to an initial condition, and, with the force measurements shown in Section 3.2.1 and the mass of the system, estimate the friction coefficient  $b$  of (3.3).

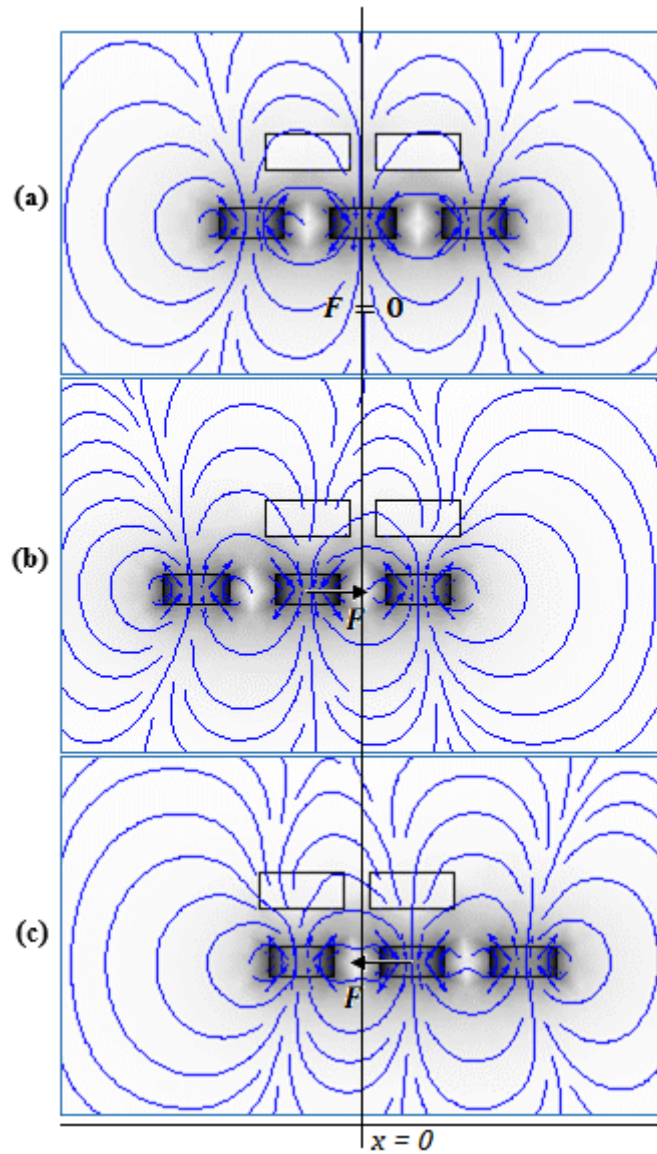


Figure 3.3: Distribution of the magnetic flux density lines and resultant forces (adapted from [15]). In a), the car is center aligned with the magnetic track, resulting in a null net force. in b) and c) there is an attractive force to the center position when the magnetic track is displaced with respect to the YBCO car.

## 3.2 Experimental Setup

An experimental rig was made to test the conditions for lateral stability shown in Figure 3.4, with the overall configuration presented in Figure 3.4a. The rig consists of a base with the mechanical rails and threaded rods (Figure 3.4b), the magnetic rail (Figure 3.4c) and the car holding the YBCO HTS bulks (Figure 3.4d).

For all experiments made, there are necessary steps that are needed to make. First, the YBCO bulks are Zero-Field Cooled. To do that, they are placed in the car, and cooled with liquid nitrogen, without the presence of a magnetic field. When the YBCO Bulk plus liquid nitrogen reach the thermal equilibrium, the YBCO bulks are superconductive. Second, the magnetic rail is positioned in the base with the mechanical rails. Last, the car is placed in the experimental rig, and tightened with nuts in the threaded



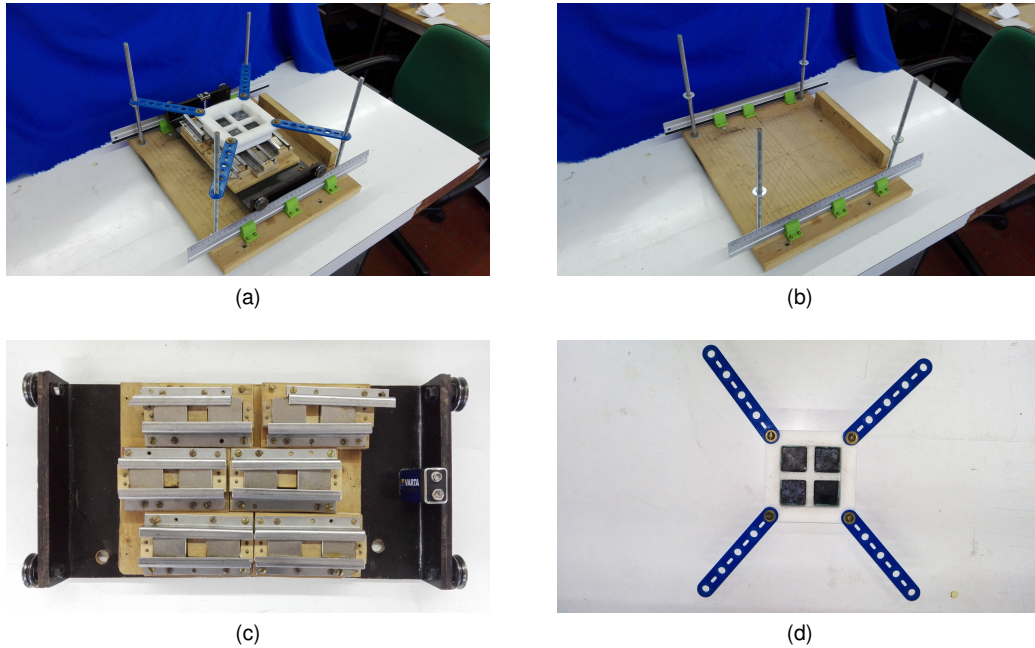


Figure 3.4: Experimental rig: a) Overall view of experimental rig b) Base of the experimental rig. c) Top view of magnetic rail. d) Top view of car which the four YBCO bulks are laid in.

rods, and with a height of 15 mm with respect to the magnetic track, as previously shown in Figure 3.1. This will make the magnetic forces align the magnetic rails (figure 3.4c) with the superconductors, and have the reference position of Figure 3.3a.

The experiments made in this setup are to determine the dynamics and the response of the car to lateral displacements. In this sense, the transient response to initial conditions of displacement was determined, and a model was developed to estimate the experimental results.

### 3.2.1 Force Field and Mass Measurement

Before conducting the experiments, measurements of the mass and the lateral forces experienced by the magnetic track were made. For the measurement of the mass, a simple scale was used, and the mass of the car is  $m = 1.8 \text{ kg}$ . For the lateral forces, a SCAIME K-12 force sensor is used to measure the lateral forces, which the datasheet is on Annex B.2. The experiment to make the measurements for the force were as following: first, the magnetic track is first displaced from the center. Second, the force sensor is placed in the opposite direction of the displacement, for it to measure the force experienced by the magnetic track. The results of this experiment and the fitting curve are shown in Figure 3.5.

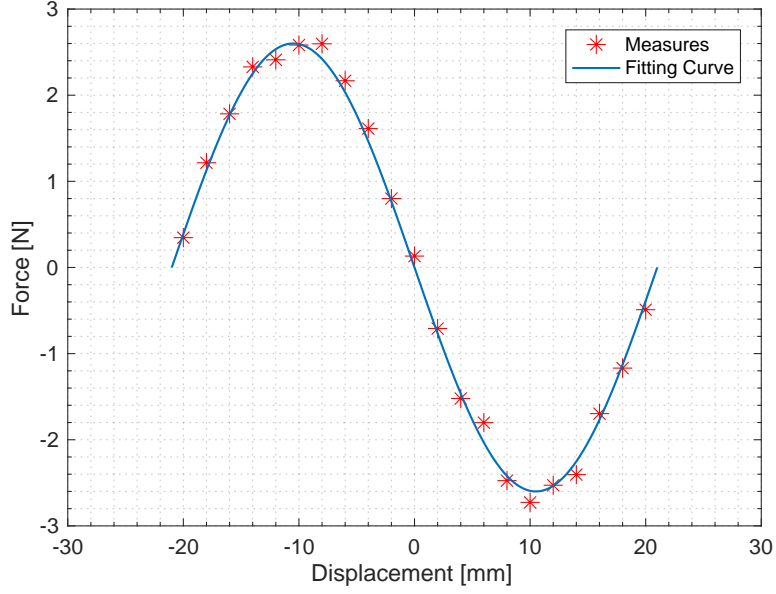


Figure 3.5: Lateral forces with respect to the lateral displacement.

The fitting used for the measurements of the magnetic force in Figure 3.5 is a sinusoidal function

$$F_{mag} = -F \sin\left(\frac{\pi}{x_{max}} x\right), \quad (3.4)$$

with a spatial period of  $43 \text{ mm}$  which corresponds with null magnetic forces in the maximum lateral displacements  $|x_{max}| = 21.5 \text{ mm}$ , and an amplitude of  $F = 2.6 \text{ N}$ . Equation (3.3) with (3.4) becomes, then:

$$m\ddot{x} + b\dot{x} + F \sin\left(\frac{\pi}{x_{max}} x\right) = 0. \quad (3.5)$$

### 3.2.2 Transient Experiment

Figure 3.6 depicts the experimental setup to test the transient conditions. The magnetic track is made to be displaced  $21 \text{ mm}$  and  $15 \text{ mm}$ , each side. Then, it is made free to move until it reaches its final position. All the motion is measured using an ultrasonic sensor, the UNAM 18U6903/S14, where the datasheet is shown in Annex B.1, and its recorded to the oscilloscope. The oscillograms of the experiments are shown in Figure 3.7.

The measurements taken from the ultrasonic sensor are in volt, having a need to convert the measured values to proper displacement values. Making a simple measure of the voltage of the sensor with respect to the displacement value, a linear regression was made:

$$x [\text{mm}] = 8.63U [\text{V}] - 8.59. \quad (3.6)$$

Using (3.6), the data is then transformed to displacement values, shown in Figure 3.8.

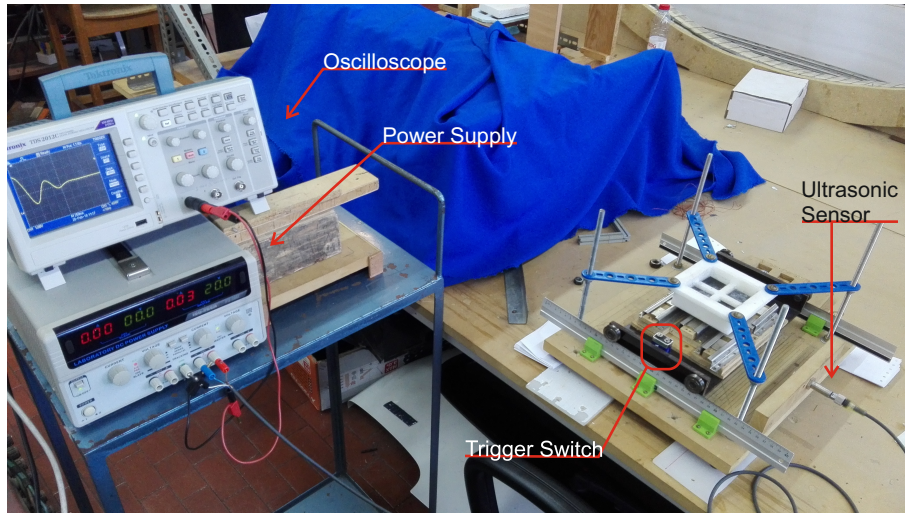


Figure 3.6: Overall view of experimental setup.

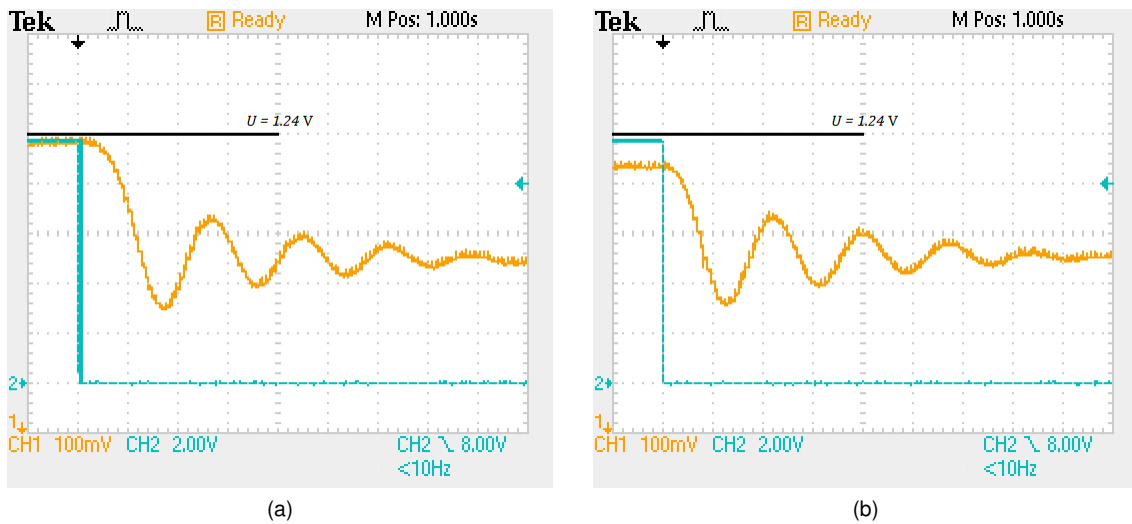


Figure 3.7: Oscillograms of the transient response to initial conditions with initial position (orange curves) of: a) 20 mm and b) 15 mm. The displacement reference is the center position. The blue curve is the trigger switch to pinpoint the start of the movement of the magnetic track.

To determine the system's dynamic function, first it is needed to estimate the friction coefficient  $b$ . Since (3.5) is a non-linear function, analytical methods based on the solution of the equation are not possible, and computation methods are required. The approach used was to sweep values for the friction coefficient  $b$ , solve equation (3.5) computationally and check the root mean square error between the experimental response and the solution of (3.5):

$$\text{RMSE} = \sqrt{\frac{1}{N} \sum_i (y_i - s_i)^2}, \quad (3.7)$$

where  $y_i$  is a sample point of the experimental response at time  $t_i$ ,  $s_i$  is a sample point of the solution of (3.5) at the same time  $t_i$  and  $N$  is the number of samples. This approach will be used for the response shown in Figure 3.7a and it will be validated using the response shown in Figure 3.7b. Figure 3.9

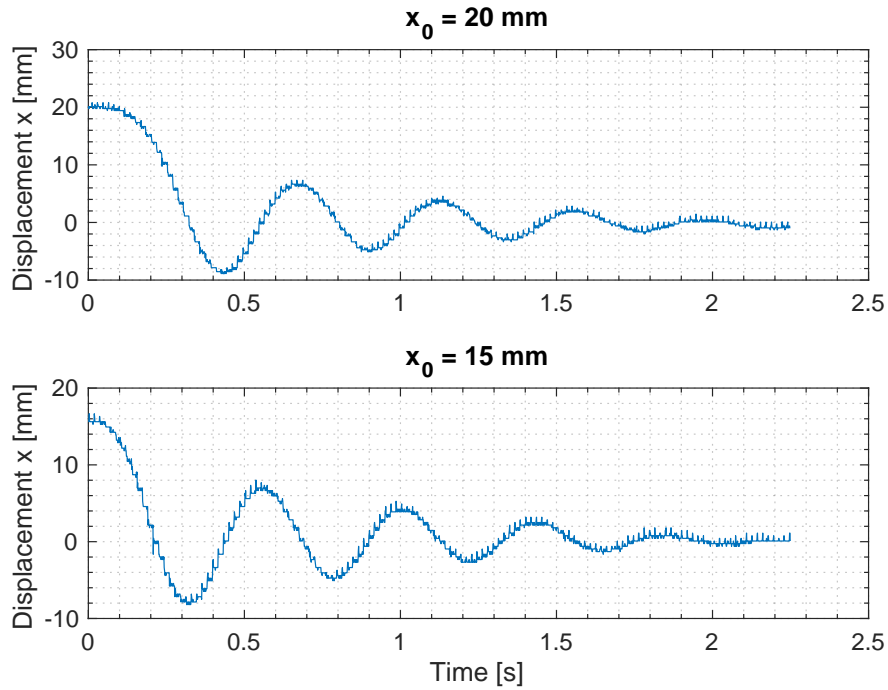


Figure 3.8: Response of the system due to a initial condition of  $x = 20 \text{ mm}$  and  $x = 15 \text{ mm}$ .

and Figure 3.10 show the value of the RMSE with respect to  $b$  and the minimum value achieved, and the estimation and validation of the solution of (3.5), respectively. The results of the validation are very similar, making this model valid to use in the dynamics of this system. Using the results of the experiment, the dynamic equation is:

$$1.88\ddot{x} + 6.1\dot{x} + 2.6 \sin\left(\frac{\pi}{0.021}x\right) = 0. \quad (3.8)$$

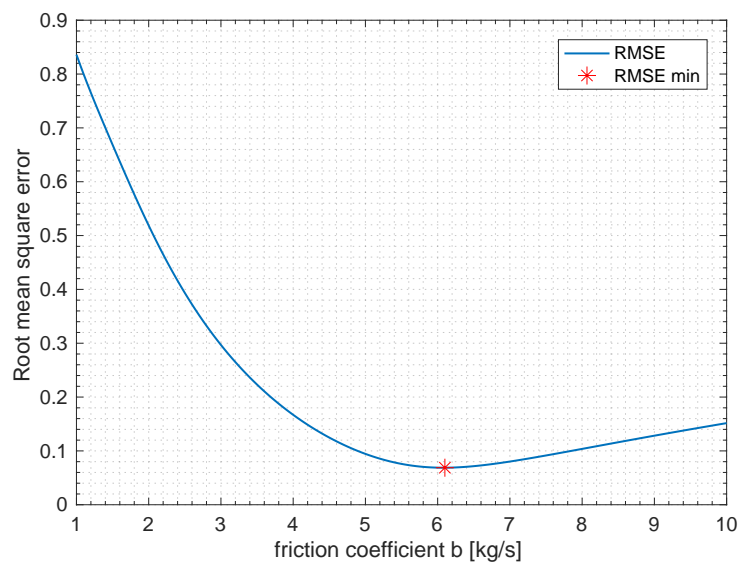


Figure 3.9: root mean square error as a function of the friction coefficient  $b$ .

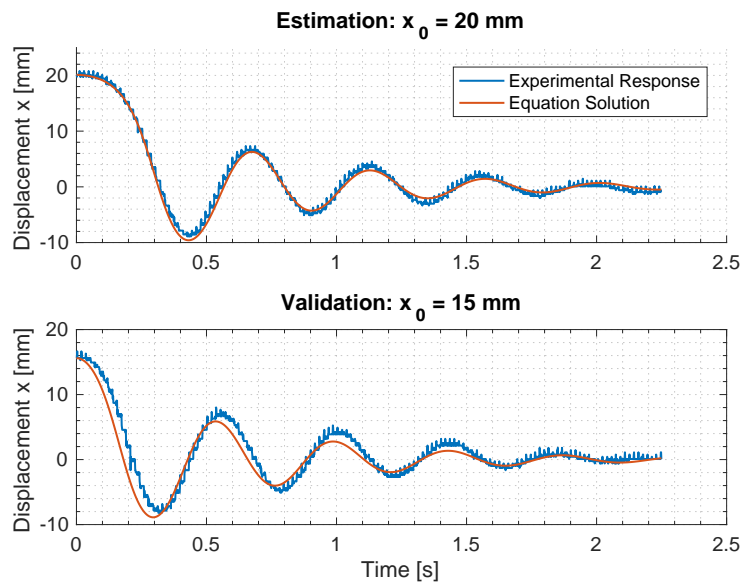


Figure 3.10: Dynamic estimated for the  $x_0 = 20 \text{ mm}$  response and the validation for the  $x_0 = 15 \text{ mm}$  response.



## **Chapter 4**

# **New HTS Cylindrical Geometry and Simulation Analysis**

In this chapter, a new HTS cylindrical geometry is analyzed concerning its use in a ZFC-Maglev vehicle. The magnetic field distribution and levitation and guidance forces are studied using a Finite Element Method (FEM) software. First, a two dimensional geometry is made. Second, taking into account manufacturing constraints, the 2D simulations are remade to satisfy the constraints and a preliminary analysis of the results is made. Third, using the results from the 2D simulations, a three dimensional geometry FEM simulation is made, and the results are compared to the 2D Simulations. Lastly, 3D simulations are made for several possible geometries for the new HTS cylindrical geometry.

## 4.1 Overview

The approach for a new ZFC-Maglev geometry is to guarantee a better lateral stability and thus better guidance for the vehicle. A proposed geometry from [2] is a cylindrical geometry. In [2], it is stated that a cylindrical geometry will behave better than the rectangular geometry of Chapter 3, regarding the lateral stability, while also using less material. In this sense, a cylindrical geometry is developed and using a finite element analysis, its magnetic field distribution and current densities are simulated to evaluate the levitation and guidance forces experienced by the HTS. The choice for a cylindrical geometry is to guarantee a more symmetrical and linear magnetic field than the one obtained in the rectangular geometry prototype. Figure 4.1 shows the conceptual design of the new magnetic circuit topology. It represents the final design the ZFC-Maglev rail. Two, or more, HTS half rings are levitating under the magnetic rail, which is made up with permanent magnets, equally distanced apart.

FEM simulations are made to determine the levitation and guidance forces of the cylindrical YBCO bulk. Since there are geometric variables that are subject to change, a study was made regarding the levitation and guidance forces with respect to the geometric variables. The levitation forces are also compared to the weight of the YBCO and the liquid nitrogen required for the cooling. This comparison is made to check what are the geometries that can guarantee levitation forces higher than the weight of the system, to guarantee they can be under additional load.

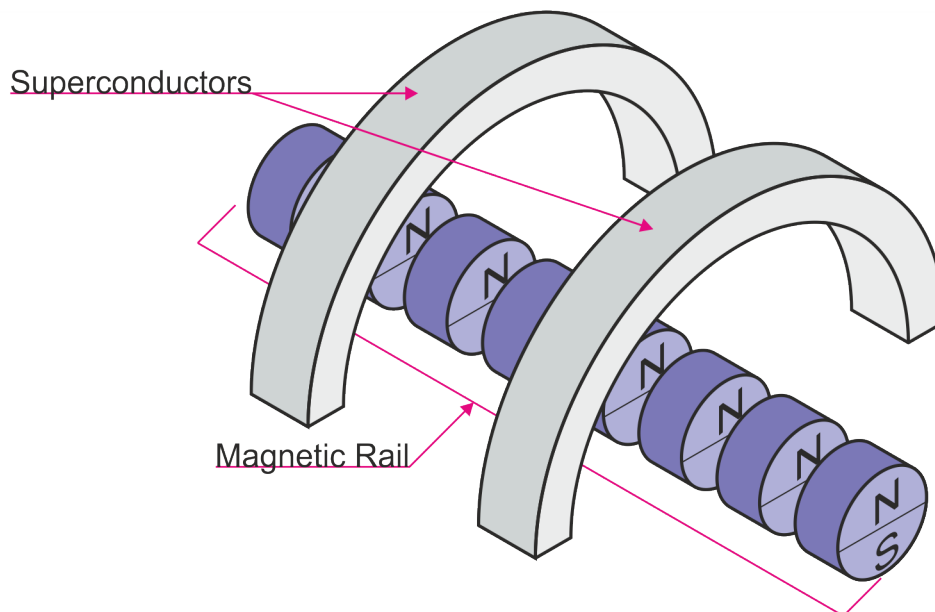


Figure 4.1: Conceptual design of the magnetic rails of the new cylindrical geometry for the ZFC-Maglev vehicle.

### 4.1.1 Geometric Description of the System

Figure 4.2 shows a representation of a HTS cylindrical block in a magnetic rail in an overall view (Fig. 4.2a) and a front view (Fig. 4.2b). There are six geometric parameters: Radius of the permanent magnet  $R_{PM}$ , depth of the PM  $D_{PM}$ , radius of the air gap  $R_{air}$ , thickness of the superconductor  $T$ ,



depth of the HTS  $D$  and spacing distance between permanent magnets  $d_{PM}$ . These are the geometric parameters used as variables in the FEM analysis, to determine the levitation and guidance forces.

For the 2D FEM simulations described in section 4.4, the model in Figure 4.2b is used, as well as the geometric parameters, for the FEM simulations. These 2D FEM Simulations set the parameters for the following 3D FEM Simulations. The 3D FEM simulations described in section 4.6 are to validate the results of the 2D simulations, and to set the parameters presented in Figure 4.2a.

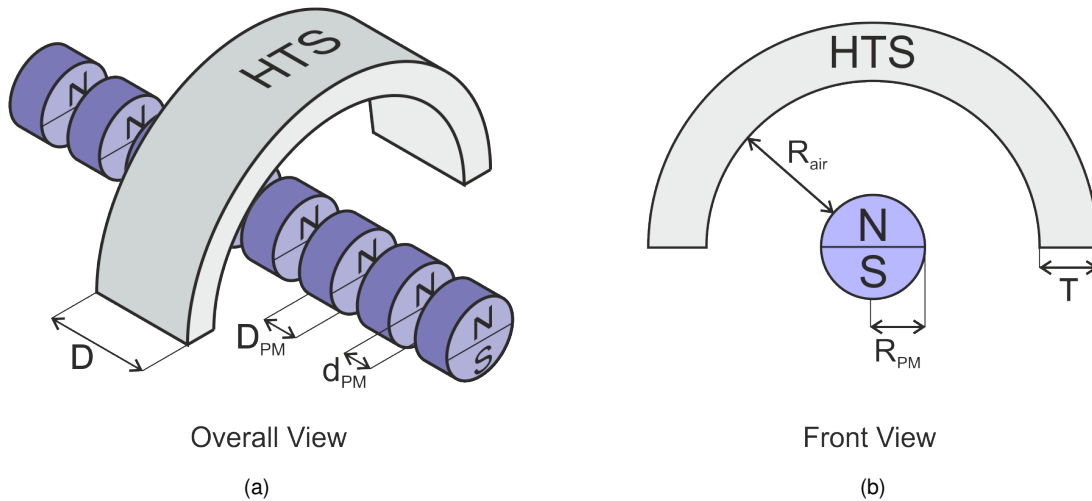


Figure 4.2: New model of the ZFC-Maglev system: a) overall view of the model and b) front view of the model (2D Representation).

## 4.2 Finite Element Method Model and Analysis

In this section, it will be described the model used in the FEM simulations and how the forces are calculated for the analysis of the cylindrical ZFC-Maglev vehicle.

### 4.2.1 H Formulation

This model is based on the H-formulation model used in [10] and [16]. The model uses the magnetic field  $\mathbf{H}$  as an independent variable, and all the constitutive relations can relate to  $\mathbf{H}$ .

For easier readability, equation (2.6) is expressed again, but using (2.3) instead of (2.5)

$$\begin{cases} \nabla \times \mathbf{E} = -\mu \frac{\partial \mathbf{H}}{\partial t} \\ \nabla \times \mathbf{H} = \mathbf{J} \\ \mathbf{E} = E_0 \left( \frac{J}{J_C} \right)^n \frac{\mathbf{J}}{J} \end{cases} \quad (4.1)$$

The equations in (4.1) are going to be described coordinate wise. Starting with Ampere's Law

$$\begin{cases} J_x = \frac{\partial H_z}{\partial y} - \frac{\partial H_y}{\partial z} \\ J_y = \frac{\partial H_x}{\partial z} - \frac{\partial H_z}{\partial x} \\ J_z = \frac{\partial H_y}{\partial x} - \frac{\partial H_x}{\partial y} \end{cases}, \quad (4.2)$$

and substituting in the E-J power law

$$\begin{cases} E_x = E_0 \left(\frac{J}{J_C}\right)^n \left(\frac{\frac{\partial H_z}{\partial y} - \frac{\partial H_y}{\partial z}}{J}\right) \\ E_y = E_0 \left(\frac{J}{J_C}\right)^n \left(\frac{\frac{\partial H_x}{\partial z} - \frac{\partial H_z}{\partial x}}{J}\right) \\ E_z = E_0 \left(\frac{J}{J_C}\right)^n \left(\frac{\frac{\partial H_y}{\partial x} - \frac{\partial H_x}{\partial y}}{J}\right) \end{cases}, \quad (4.3)$$

where  $J$  is the norm of the current density, which is also a function of the magnetic field

$$J = \sqrt{\left(\frac{\partial H_z}{\partial y} - \frac{\partial H_y}{\partial z}\right)^2 + \left(\frac{\partial H_x}{\partial z} - \frac{\partial H_z}{\partial x}\right)^2 + \left(\frac{\partial H_y}{\partial x} - \frac{\partial H_x}{\partial y}\right)^2}. \quad (4.4)$$

For the Faraday's law, one has, coordinate wise

$$\begin{cases} \frac{\partial H_x}{\partial t} = \frac{1}{\mu} \left(\frac{\partial E_z}{\partial y} - \frac{\partial E_y}{\partial z}\right) \\ \frac{\partial H_y}{\partial t} = \frac{1}{\mu} \left(\frac{\partial E_x}{\partial z} - \frac{\partial E_z}{\partial x}\right) \\ \frac{\partial H_z}{\partial t} = \frac{1}{\mu} \left(\frac{\partial E_y}{\partial x} - \frac{\partial E_x}{\partial y}\right) \end{cases}, \quad (4.5)$$

and using (4.3) and (4.4), one has the complete description of the system in terms of the magnetic field, coordinate wise.

## 4.2.2 Maxwell Stress Tensor and Force Calculation

Starting with the Lorentz Force considering a charge  $q$  moving through a magnetic field, of magnetic flux density  $\mathbf{B}$ , with velocity  $v$

$$\mathbf{F} = q\mathbf{v} \times \mathbf{B}, \quad (4.6)$$

the force density  $\mathbf{f}$  can be obtained from (4.6) by summing all the forces experienced in a small volume. Mathematically, it is written as

$$\mathbf{f} = \lim_{\delta V \rightarrow 0} \frac{\sum_i \mathbf{F}_i}{\delta V} = \lim_{\delta V \rightarrow 0} \frac{\sum_i q_i \mathbf{v}_i \times \mathbf{B}_i}{\delta V}, \quad (4.7)$$

where  $\mathbf{F}_i$ ,  $q_i$  and  $\mathbf{v}_i$  are the force, charge and velocity of the  $i$ th particle in the volume  $\delta V$  and  $\mathbf{B}_i$  is the flux density experienced by the  $i$ th particle. If one can assume that all the particles within  $\delta V$  experience

the same flux density  $\mathbf{B}$ , one can use the definition of current density

$$\mathbf{J} = \lim_{\delta V \rightarrow 0} \frac{\sum_i q_i \mathbf{v}_i}{\delta V}, \quad (4.8)$$

to write (4.7) as

$$\mathbf{f} = \mathbf{J} \times \mathbf{B}. \quad (4.9)$$

This approximation can be made because the volume  $\delta V$  can be made small enough to enclose a region of essentially constant magnetic flux, still including many free charges.

Using (4.9) to calculate the force density is a difficult process, since it is needed to know the current distribution of the solid. The force density can be only expressed using only field quantities. With the constitutive relation (??) and Ampere's law (2.1c), (4.9) can be written in the form

$$\mathbf{f} = \mu (\nabla \times \mathbf{H}) \times \mathbf{H}. \quad (4.10)$$

It is a vector identity that this expression can be written as <sup>1</sup>

$$\mathbf{f} = \mu (\mathbf{H} \cdot \nabla) \mathbf{H} - \frac{\mu}{2} \nabla (\mathbf{H} \cdot \mathbf{H}). \quad (4.11)$$

The description of the force field  $\mathbf{f}$  usually is not made component wise, but in this case, there are some manipulations that are easier to perform component by component. For this mathematical operations, the expressions at hand will be dealt using *index notation*.

For the following analysis, some assumptions are to be made. First, a right-hand cartesian coordinate system  $x_1, x_2, x_3$  (it is the same as  $x, y, z$ ) is assumed. The component of a vector in the direction of an axis carries the subscript of that axis. This means that  $f_m$  is the  $m$ th component of the vector  $\mathbf{f}$ , where  $m$  can be 1, 2 or 3. The differential operator  $\partial/\partial x_n$  can be  $\partial/\partial x_1, \partial/\partial x_2$  or  $\partial/\partial x_3$ . Second, when the index is repeated in a single term, it implies summation over the three values of the index

$$\frac{\partial H_n}{\partial x_n} = \frac{\partial H_1}{\partial x_1} + \frac{\partial H_2}{\partial x_2} + \frac{\partial H_3}{\partial x_3} = \nabla \cdot \mathbf{H} \quad (4.12)$$

and

$$H_n \frac{\partial}{\partial x_n} = H_1 \frac{\partial}{\partial x_1} + H_2 \frac{\partial}{\partial x_2} + H_3 \frac{\partial}{\partial x_3} = \mathbf{H} \cdot \nabla. \quad (4.13)$$

This equations illustrate the *summation convention* or *Einstein convention*. If one wants to represent one of the nine possible derivative of components of  $\mathbf{H}$ , one writes  $\partial H_m / \partial x_n$ .

Third, the *Kronecker delta*  $\delta_{mn}$  is defined as

$$\delta_{mn} = \begin{cases} 1, & \text{if } m = n \\ 0, & \text{if } m \neq n \end{cases}, \quad (4.14)$$

---

<sup>1</sup>  $(\nabla \times \mathbf{A}) \times \mathbf{A} = (\mathbf{A} \cdot \nabla) \mathbf{A} - \frac{1}{2} \nabla (\mathbf{A} \cdot \mathbf{A})$

and, using the *summation convention*, has the properties

$$\delta_{mn}H_n = H_m \quad (4.15)$$

and

$$\delta_{mn} \frac{\partial}{\partial x_n} = \frac{\partial}{\partial x_m}, \quad (4.16)$$

which can be verified by using the definition (4.14).

With these definitions, one can write the  $m$ th component of (4.10) as

$$f_m = \mu H_n \frac{\partial H_m}{\partial x_n} - \frac{\mu}{2} \frac{\partial}{\partial x_m} (H_k H_k). \quad (4.17)$$

With the property of the Kronecker delta ( $\partial/\partial x_m = \delta_{mn}(\partial/\partial x_n)$ ) and some manipulation, one can write (4.17) as

$$\begin{aligned} f_m &= \mu H_n \frac{\partial H_m}{\partial x_n} - \frac{\mu}{2} \frac{\partial}{\partial x_m} (H_k H_k) + \mu H_m \frac{\partial H_m}{\partial x_n} - \mu H_m \frac{\partial H_m}{\partial x_n} \\ &= \frac{\partial}{\partial x_n} \left( \mu H_n H_m - \frac{\mu}{2} \delta_{mn} H_k H_k \right) - H_m \frac{\partial \mu H_n}{\partial x_n}. \end{aligned} \quad (4.18)$$

The last term on the right is (remembering the *summation convention*) the divergence of the magnetic field

$$H_m(\nabla \cdot \mu \mathbf{H}) = H_m(\nabla \cdot \mathbf{B}) = 0,$$

and this in turn gives a concise form to write (4.17) as

$$f_m = \frac{\partial T_{mn}}{\partial x_n}, \quad (4.19)$$

where  $T_{mn}$  is the Maxwell stress tensor and is given by

$$T_{mn} = \mu H_n H_m - \frac{\mu}{2} \delta_{mn} H_k H_k. \quad (4.20)$$

Looking at (4.20), once can see that the Maxwell stress tensor  $T_{mn}$  is a function of only the total magnetic field  $\mathbf{H}$ . A conclusion made is that the force density  $\mathbf{f}$  can be calculated using only the magnetic field.

To find the  $m$ th component of the total force  $\mathbf{F}$ , the volume integration of the force density is made:

$$F_m = \iiint_V f_m dV = \iiint_V \frac{\partial T_{mn}}{\partial x_n} dV. \quad (4.21)$$

If the components of a vector  $\mathbf{A}$  are defined as

$$A_1 = T_{m1}, \quad A_2 = T_{m2}, \quad A_3 = T_{m3}, \quad (4.22)$$

(4.21) becomes

$$F_m = \iiint_V \frac{\partial A_n}{\partial x_n} dV = \iiint_V (\nabla \cdot \mathbf{A}) dV \quad (4.23)$$

Using the divergence theorem, one arrives to the conclusion that the total force is a surface integral of the stress tensor:

$$F_m = \iint_S (\mathbf{A} \cdot \mathbf{n}_S) dS = \iint_S A_n (n_n)_S dS, \quad (4.24)$$

where  $n_n$  is the  $n$ th component of the outward-directed unit vector  $\mathbf{n}$  normal to the surface  $S$  and the surface  $S$  encloses the volume  $V$ . Using (4.22) to substitute back to (4.24) yields

$$F_m = \iint_S T_{mn} (n_n)_S dS. \quad (4.25)$$

It is with (4.25) that the forces are calculated in the simulations.

### 4.2.3 Application Example of the Maxwell Stress Tensor

For matter of example, consider applying (4.25) on a cubic volume  $V$ . The integrand  $T_{mn}n_n$ , in view of the summation convention, is the  $m$ th component of a vector. This vector has the name traction and a symbol  $\tau$ . Thus the  $m$ th component of the traction is written as

$$\tau_m = T_{mn}n_n = T_{m1}n_1 + T_{m2}n_2 + T_{m3}n_3. \quad (4.26)$$

Figure 4.3 presents the cubic volume in question, with the top, bottom and right normal vectors to the top, bottom and right surfaces, respectively. For this example, let us consider that this is a small enough cubic volume  $V$ , such that there is no change in the Maxwell stress tensor  $T_{mn}$  over one face. With this in mind for the calculation of (4.25), one needs to calculate for each surface, i.e., for each normal of the surface in choice. Considering the top surface, which has a normal  $n^t$

$$n_1^t = 0, \quad n_2^t = 0, \quad n_3^t = 1,$$

and the traction for the top surface  $\tau^t$  is, then:

$$\tau_1^t = T_{13}, \quad \tau_2^t = T_{23}, \quad \tau_3^t = T_{33}.$$

For the bottom surface, since the normal  $n^b$  is

$$n_1^b = 0, \quad n_2^b = 0, \quad n_3^b = -1,$$

the traction for the bottom surface is:

$$\tau_1^b = -T_{13}, \quad \tau_2^b = -T_{23}, \quad \tau_3^b = -T_{33}.$$

For the right surface, the normal  $n^r$

$$n_1^r = 0, \quad n_2^r = 1, \quad n_3^r = 0,$$

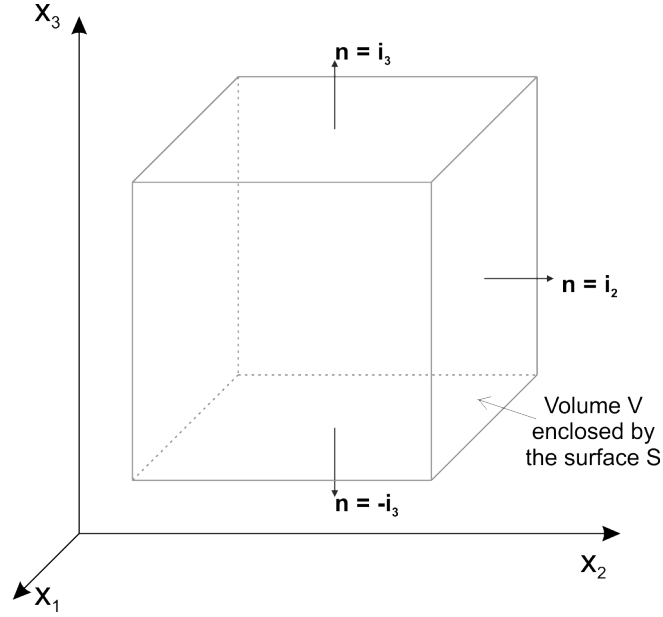


Figure 4.3: Example of cubic volume  $V$  enclosed by the surface  $S$ , displaying the top, bottom and right normal of the surface.

the traction for the bottom surface is:

$$\tau_1^r = T_{11}, \quad \tau_2^r = T_{21}, \quad \tau_3^r = T_{31}.$$

This means that the elements of the traction depend on what and where is the normal, and the  $m$ th component of a force depends on all the  $m$ th components of the traction. In mathematical terms, and for this example, this means that the  $m$ th component of the force  $F_m$  is:

$$F_m = \iint_{S^t} \tau_m^t dS^t + \iint_{S^b} \tau_m^b dS^b + \iint_{S^l} \tau_m^l dS^l + \iint_{S^r} \tau_m^r dS^r + \iint_{S^f} \tau_m^f dS^f + \iint_{S^{bk}} \tau_m^{bk} dS^{bk}, \quad (4.27)$$

where t,b,l,r,f,bk, represent top, bottom, left, right, front and back, respectively. Using the fact that all the components of the traction  $\tau$  are the stress tensor  $T_{mn}$  or its inverse value  $-T_{mn}$ , then (4.27) can be described as the sum of the products of the stress tensor with the surface area  $S$

$$F_m = S (T_{m3}^t - T_{m3}^b) + S (T_{m2}^r - T_{m2}^l) + S (T_{m1}^f - T_{m1}^{bk}). \quad (4.28)$$

Figure 4.4 illustrates the tensors in each face of the cubic volume. Tensors of the same color represent the contributions to the force of the same direction. the ones in the same, but lighter color, represent the contributions in the opposite direction.

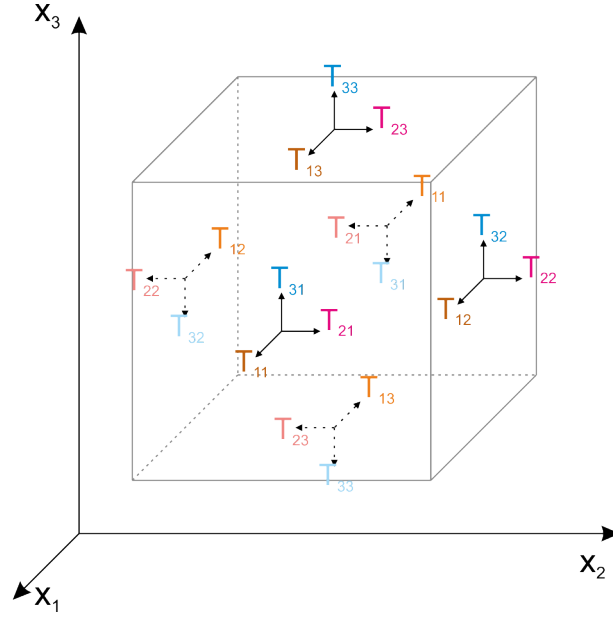


Figure 4.4: Example of cubic volume  $V$  enclosed by the surface  $S$ , displaying the tensors in each face.

### 4.3 Material Characteristics

For the simulation of the system, the electromagnetic, mechanical and geometric properties of the YBCO and the permanent magnets of the magnetic rail must be specified.

For the YBCO HTS, the electromagnetic parameters needed are the ones used in the E-J power law, shown in (2.3):  $E_0$ ,  $B_0$ ,  $J_{C0}$  and  $n$ . The electromagnetic values used for the simulations are taken from [11]. For the mechanical values, the density is needed for the calculation of the mass and the weight of the YBCO. The density was measured using the YBCO bulks used in the system of Chapter 3. These parameters are shown in Table 4.1.

Table 4.1: Electromagnetic and mechanical parameters of the YBCO Bulk.

Electromagnetic Par.		Values
$E_0$	$\text{Vm}^{-1}$	$1 \cdot 10^{-4}$
$B_0$	$[\text{T}]$	0.1
$J_{C0}$	$\text{Am}^{-2}$	$1.82 \cdot 10^8$
$n$		30
Mechanical Par.		-
$\rho_{YBCO}$	$\text{kg m}^{-3}$	$5.81 \cdot 10^3$

The geometric parameters are needed to calculate the area, volume and, consequently, the weight of the YBCO. Figure 4.2b is shown again here, in Figure 4.5, for easier readability.

Using the variables in Figure 4.5, the inner and outer radius of the YBCO Bulk,  $r_{in}$  and  $r_{out}$ , respectively, can be derived as:

$$\begin{cases} r_{in} = D_{PM}/2 + R_{air} \\ r_{out} = r_{in} + T = D_{PM}/2 + R_{air} + T \end{cases} \quad (4.29)$$

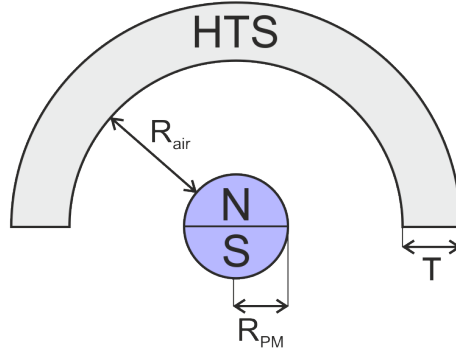


Figure 4.5: Front view of YBCO half ring bulk with the magnetic rail.

The area of the YBCO bulk is, then:

$$A_{bulk} = \frac{\pi}{2} (T + 2r_{in}) T. \quad (4.30)$$

For the volume of the half ring, (4.30) is multiplied by the depth  $D$

$$V_{bulk} = \frac{\pi}{2} (T + 2r_{in}) TD, \quad (4.31)$$

and using the density of the YBCO, its mass and weight are, then:

$$\begin{cases} m_{YBCO} = V_{YBCO} \rho_{YBCO} \\ F_g = V_{YBCO} \rho_{YBCO} g \end{cases}. \quad (4.32)$$

For the permanent magnets, the magnetization curve is

$$B_{PM} = \mu_0 \mu_{rPM} H_{PM} + B_r, \quad (4.33)$$

where  $B_r$  is the remanent flux density and  $\mu_{rPM}$  is the relative permeability of the permanent magnets.

Table 4.2 shows the electromagnetic and geometric parameters of the PM.

Table 4.2: Electromagnetic and geometric parameters of the permanent magnets.

Electromagnetic Par.	Values
$B_r$ [T]	1.2
$\mu_{rPM}$	1.05
Mechanical Par.	-
$R_{PM}$ [mm]	12.5
$D_{PM}$ [mm]	14



## 4.4 2D Distributed Parameters Model

For the 2D analysis, there are some considerations to make: first, along the z axis, which is the axis along the depth of the model, the electromagnetic results do not change. This means, for example, that the magnetic flux dispersion is only considered along the x and y axis, and not the z axis. Second, the depth of the model is set to  $D = 1$  m. This means that the PM and the YBCO have the same depth, and there is no piecewise magnetic rail, but a continuous cylindrical PM and the forces computed can be considered as a force density, along the z axis. In the following sections, the 2D FEM analysis model description and results are shown.

### 4.4.1 2D FEM Model

As it was described in section 4.2.1, the FEM software uses the magnetic field formulation to solve (2.7) from Section 2.4.2 and this equation has a time derivative. This means that this equation needs initial conditions to be solved. To do this, the main simulation is made by making a step function of the magnetic field of the PM. This simulates the already ZFC YBCO being put near the permanent magnets. Figure 4.6 shows a schematic of the model used in the FEM software and Figure 4.7 shows the initial conditions of the simulation, which is a step function of the remanent magnetic field in the y direction.

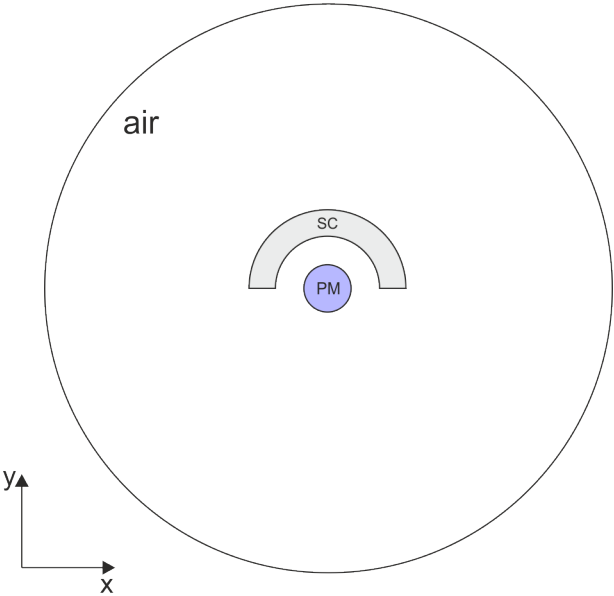


Figure 4.6: Schematic of the cylindrical ZFC-Maglev geometric model used in the 2D electromagnetic simulations.

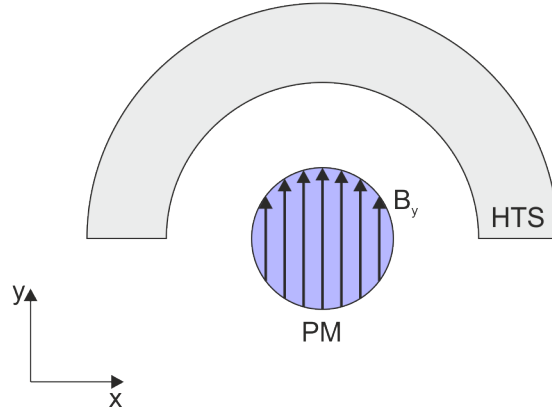


Figure 4.7: Initial conditions and representation of the magnetization direction in the PM used in the 2D simulations.

This simulation uses a 2D model of the geometry, and so, the H formulation described in Section 4.2.1 has a different form. In 2D models,  $\mathbf{H}$  only has  $x$  and  $y$  components, and there is no change in the  $z$  direction, which means that  $\partial/\partial z = 0$ . This makes (4.2) have the following form:

$$\begin{cases} J_x = 0 \\ J_y = 0 \\ J_z = \frac{\partial H_y}{\partial x} - \frac{\partial H_x}{\partial y} \end{cases} . \quad (4.34)$$

Consequently, the electric field in (4.3) only has a  $z$  component

$$E_z = E_0 \left( \frac{\frac{\partial H_y}{\partial x} - \frac{\partial H_x}{\partial y}}{J_C} \right)^n , \quad (4.35)$$

and Faraday's law becomes

$$\begin{cases} \frac{\partial H_x}{\partial t} = -\frac{E_0}{J_C^n} \frac{\partial}{\partial y} \left( \frac{\partial H_y}{\partial x} - \frac{\partial H_x}{\partial y} \right)^n \\ \frac{\partial H_y}{\partial t} = \frac{E_0}{J_C^n} \frac{\partial}{\partial x} \left( \frac{\partial H_y}{\partial x} - \frac{\partial H_x}{\partial y} \right)^n \end{cases} . \quad (4.36)$$

#### 4.4.2 Physical Interpretation of the 2D Simulation using FEM

Figure 4.8 shows the results of the electromagnetic model of the HTS, using the initial conditions shown in Figure 4.7. Analyzing the magnetic vector field, it is visible that the HTS is repelling the magnetic field of the PM. This is a consequence of the current density distribution in the HTS. The current density only has the  $z$  component, and the currents are in a closed loop, creating, by Ampère's law, an opposite magnetic field. This creates a null resultant magnetic field in the surface of the superconductor. However, this is not a completely repulsive behavior, and there is some field penetration in the HTS, as it can be seen in Figure 4.8.

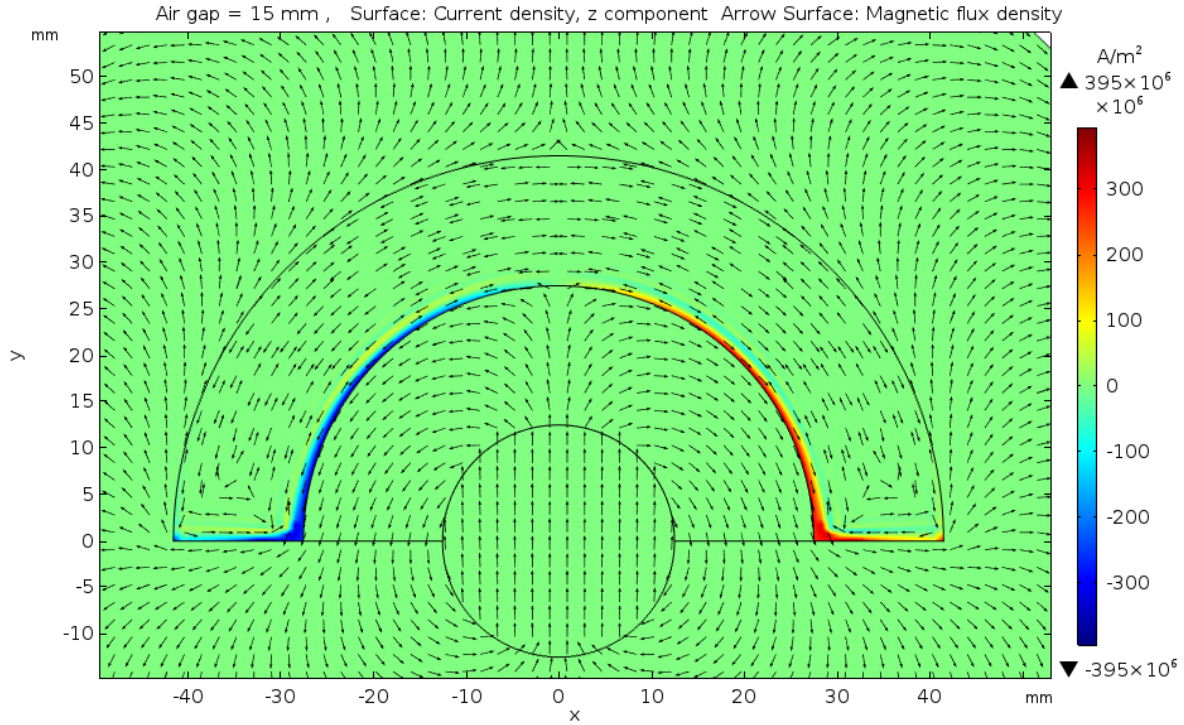


Figure 4.8: Results of the simulation. Here, the surface current density in the z component are shown in the color graph, and the black arrows are the magnetic vector field.

#### 4.4.3 2D FEM Simulations for the Calculation of the Levitation Force $F_y$

The first simulations made are to compute the levitation force  $F_y$  of the HTS, by making a parametric sweep of the thickness  $T$  and the air gap  $R_{air}$ , making all of the possible combinations between the variables. Table 4.3 shows the values for the parametric sweep. With these values,  $F_y$  is computed for each air gap and thickness. Figure 4.9 shows a graphic of the results of the levitation force  $F_y$  with respect to the air gap, for different thicknesses. These results show that the levitation forces are similar for different thicknesses, especially for air gaps greater than 10 mm.

Table 4.3: Values of the geometric variables for the parametric sweep.

Variables	Values [mm]
$T$	(7, 10, 14, 16)
$R_{air}$	from 1 to 30, in steps of 1

Regarding the air gap, the best function that fitted the data of  $F_y$  is the function

$$f_{fit}(x) = ae^{bx^2+cx}. \quad (4.37)$$

Figure 4.10 shows the graph of the fitting curve and the data of  $F_y$  with respect to the air gap. Since the results are similar for each thickness, it is only displayed the simulation with a thickness of 10 mm, the values for equation (4.37) are:

$$a = 3.67 \cdot 10^3, \quad b = 1.8 \cdot 10^{-3}, \quad c = -0.17,$$

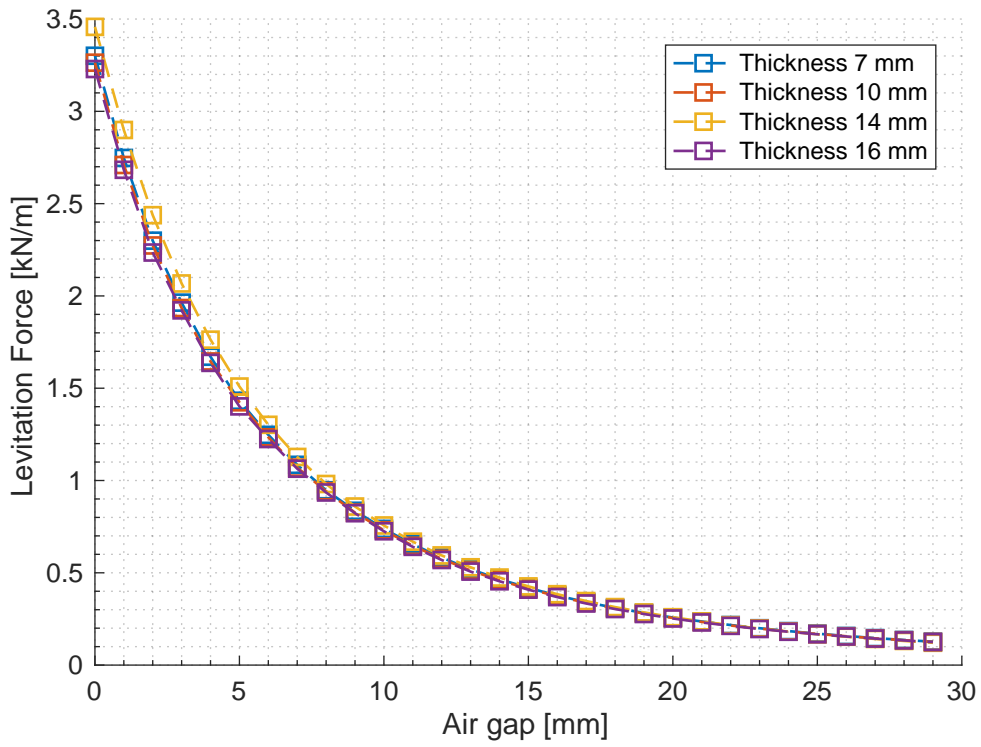


Figure 4.9: Levitation Force computed in the 2D simulations for different air gap and thickness values of the YBCO.

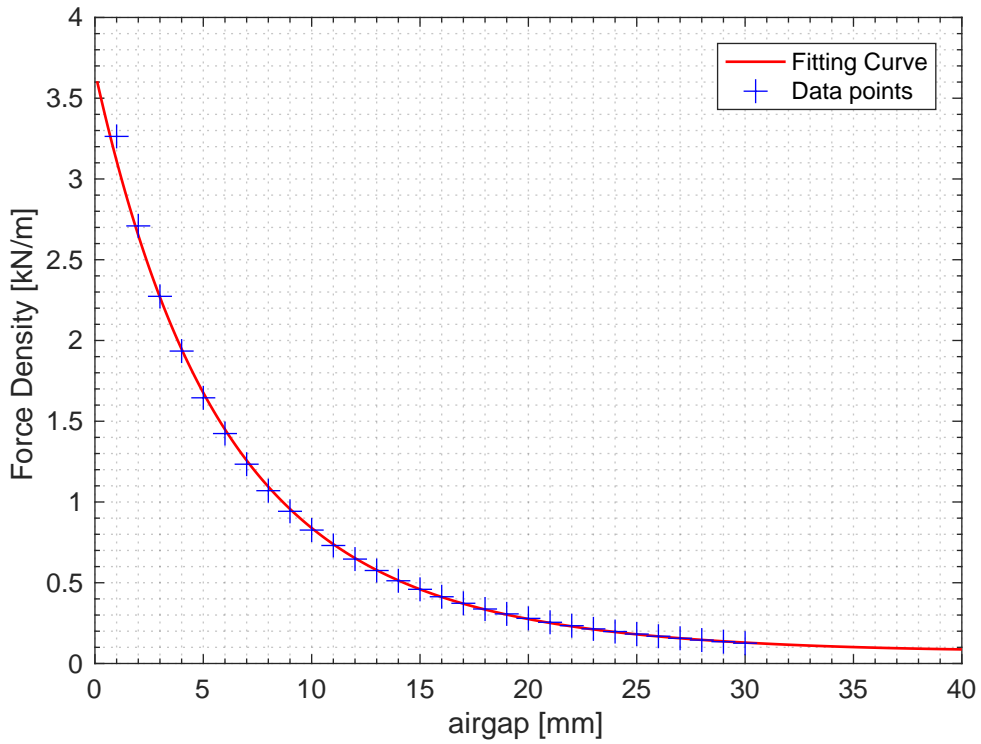


Figure 4.10:  $F_y$  Data and the fitting curve.

#### 4.4.4 Calculation of the Equilibrium Force $F_{Eq}$

With (4.32) and (4.37), the weight of the YBCO and the air gap value resulting in a null resultant force was calculated, respectively. The results are shown in Table 4.4. An important fact to notice is that the fitting function (4.37) is convex, and this behavior of the function does not correspond to the actual physics of the model, since the value of the force goes to zero as the air gap increases. Table 4.4 also shows the value of the minimum of each fitting function. Only for a thickness of 7 mm that the air gap value was higher than the minimum, which makes the result invalid to use. To surpass this, a new simulation would need to be made, with larger air gaps. However, this study is not made, due to the manufacturing constraints, explained in section 4.5.

Table 4.4: Results for the air gap value for null resultant force, for each thickness, and the minimum of the fitting curve.

Thickness [mm]	Air gap [mm]	Function minimum [mm]	Equilibrium Force [N]
7	50.1	46.0	82
10	36.4	46.0	97
14	30.1	48.1	125
16	28.5	46.0	141

## 4.5 Manufacturing and Budget Constraints: New Model and Second Simulation

One of the initial objectives of this dissertation was to make a functional prototype of the new geometry considered in this chapter. In order to fulfill this requirement, a quotation was sent to CAN Superconductors for the HTS with different thicknesses. In reply, CAN stated that they can only manufacture HTS with a thickness of  $T = 10$  mm and a maximum depth of  $D = 40$  mm and, for this geometry, the half ring is divided in 6 equal pieces.

### 4.5.1 Piecewise HTS FEM Model

Using the results of section 4.4.4 and the manufacturing constraint, a new 2D model was made for the FEM Analysis, shown in Figure 4.11.

The first simulation made is to verify if there is an influence on the levitation force regarding the YBCO being made with 6 bulks, instead of a complete one. On the simulations, this is made by making a discontinuity on the distribution of current between the YBCO bulk pieces. The levitation force of this experiment was of 95.5 N and it presents a deviation from the result of table 4.4 of 1.6 %, which is negligible. This confirms that it is plausible to have the same levitation forces and the same behavior being the YBCO a piecewise or a continuous half-ring bulk.

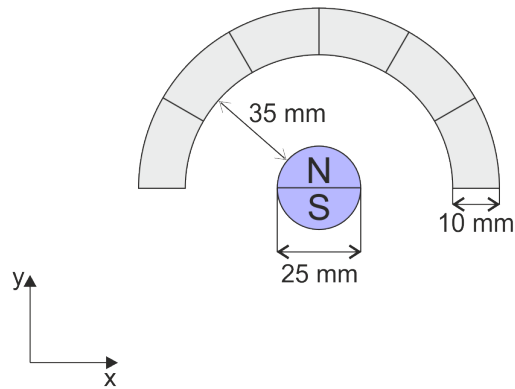
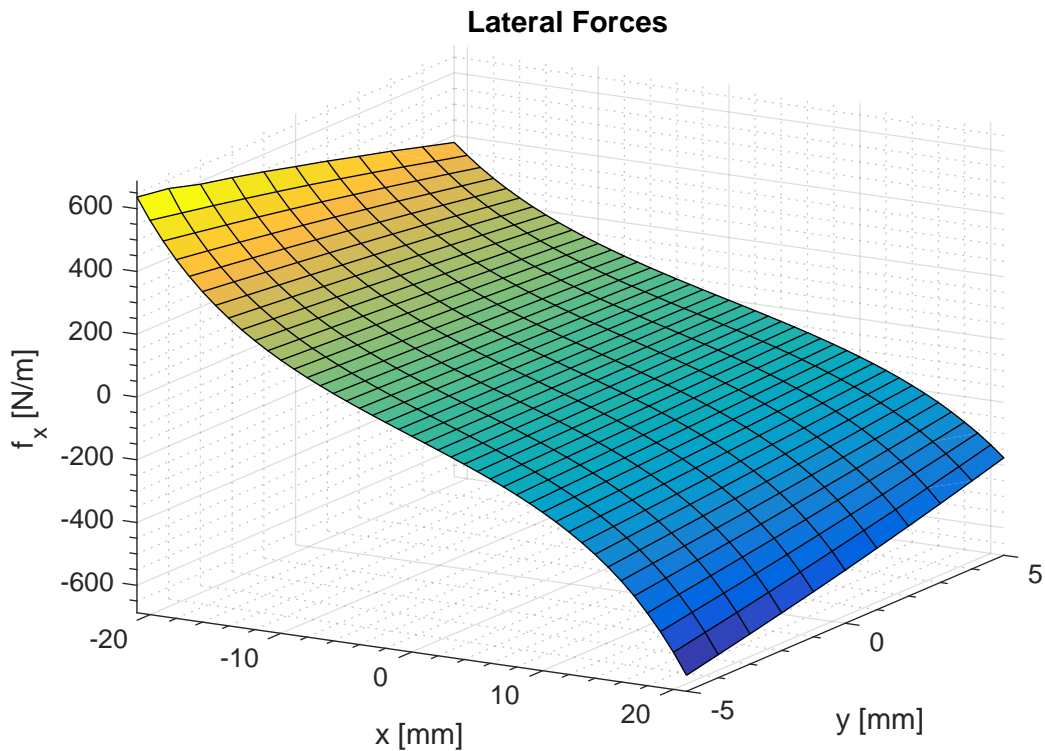


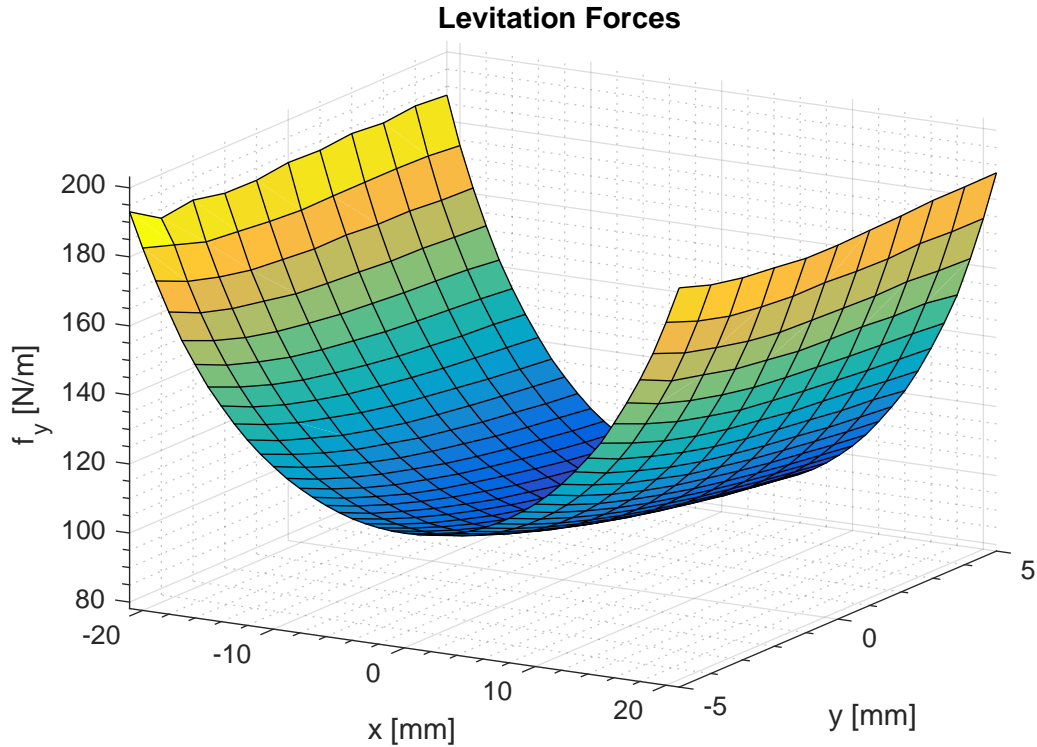
Figure 4.11: Representation of the new geometry, satisfying the manufacturer constraints.

#### 4.5.2 2D FEM simulations of the New Piecewise HTS and Computation of the Levitation and Lateral Forces

The next simulation made is a parametric sweep regarding translations of the HTS. This simulation computes the levitation and lateral forces,  $F_y$  and  $F_x$  respectively. Figure 4.12 shows the results of  $F_y$  and  $F_x$  with respect to the coordinate pair  $(x, y)$ . In Chapter 5, the results of this simulation will be compared with the results of Chapter 3, regarding the stability of both geometries.



(a)



(b)

Figure 4.12: 2D results of the Forces computed: a) Guidance Forces. b) Levitation Forces.

## 4.6 3D Distributed Parameter Model

In comparison with the 2D FEM analysis, the 3D FEM analysis will have in consideration all the variables in all the axes, e.g, the magnetic flux dispersion will happen in  $x$ ,  $y$  and  $z$ . Also the depth is not fixed as it is in the 2D analysis, meaning that it is set a depth for the magnetic track, either being a continuous PM or a piecewise magnetic track, and the simulations will also focus on the possible depths of the YBCO. In the following sections, the 3D FEM analysis model description and results are shown.

### 4.6.1 3D FEM Model

For the 3D simulations, the model used is shown in Figure 4.13. For the simulations made, the magnetic track needs to be able to be made of a continuous cylindrical PM, or made with several PM, equally spaced apart. To address this property and maintain only on FEM model, the magnetic track was made with several PM, and when the spacing between them is null, it is regarded in the simulations as if it is a continuous cylindrical tube.

Figure 4.13 shows the initial conditions of the 3D simulations. It follows the same procedure as the 2D FEM simulations: the main simulation is made by making a step function of the magnetic field of the PM. This simulates the already ZFC YBCO being put near the permanent magnets. The remanent magnetic field is in the  $z$  direction.

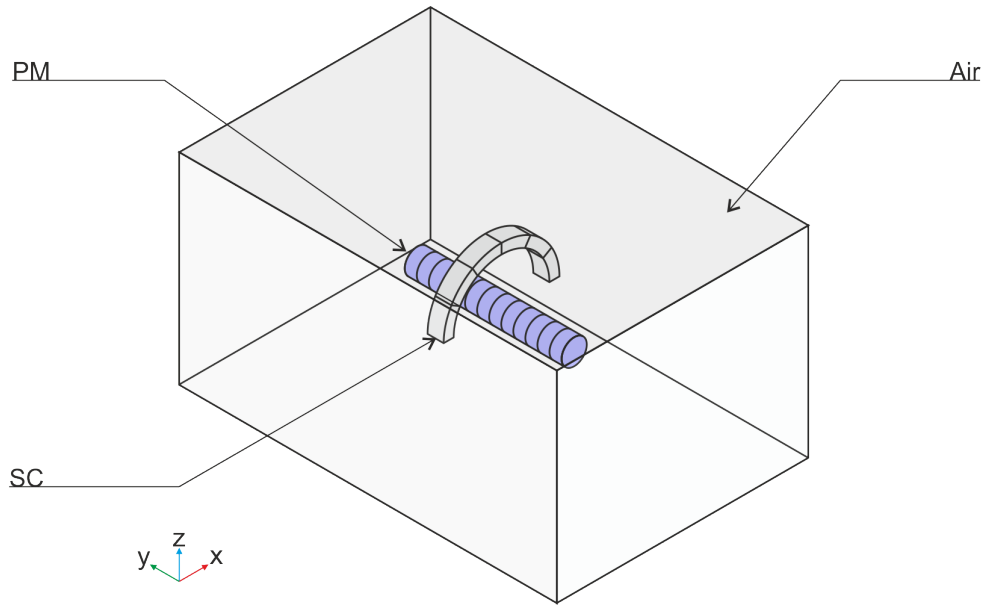


Figure 4.13: Schematic of the cylindrical ZFC-Maglev geometric model used in the 3D electromagnetic simulations.

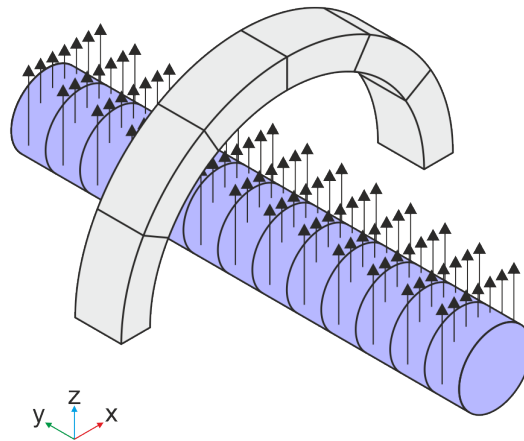


Figure 4.14: Initial conditions and representation of the magnetization direction in the PM used in the 3D simulations.

#### 4.6.2 3D FEM Simulations for the Calculation of the Levitation Force and Comparison with the 2D Results

The first 3D FEM simulation is made to compare the value of the levitation force computed  $F_{lev3D}$  with the computed in the 2D simulations of Section 4.4.4. The simulation consists of a parametric sweep of the depth  $D$  of the YBCO bulk for the calculation of the levitation force  $F_{lev3D}$ . Table 4.5 shows the geometric parameters used for the simulation. Note that the thickness is set to  $T = 10$  mm because of the manufacturing constraints imposed, and the distance between permanent magnets is  $d_{PM} = 0$  mm since the comparison between the 2D and 3D levitation forces is only valid considering a continuous cylindrical PM tube.



Table 4.5: Values of the geometric variables used for the comparison between the 2D and 3D levitation forces.

Variables	Values [mm]
$R_{air}$	35
$T$	10
$D$	(16, 20, 24, 28, 32, 36, 40)
$d_{PM}$	0

For the levitation force  $F_{lev2D}$ , one uses the levitation force density  $f_{lev2d}$  computed in Section 4.4.4 shown on Table 4.4. The levitation force  $F_{lev2D}$  for each depth  $D$  is

$$F_{lev2D} = f_{lev2D}D. \quad (4.38)$$

The 2D and 3D levitation forces for each depth are shown in Table 4.6, as well as the error between them

$$error[\%] = \frac{|F_{lev3D} - F_{lev2D}|}{F_{lev3D}} \cdot 100. \quad (4.39)$$

Table 4.6: Comparison between the values of the levitation forces in the 2D and 3D simulations.

Depth [mm]	$F_{lev3D}$ [N]	$F_{lev2D}$ [N]	Error [%]
16	1.03	1.55	51.3
20	1.40	1.94	38.1
24	1.83	2.33	27.5
28	2.25	2.72	20.7
32	2.71	3.10	14.6
36	3.14	3.49	11.0
40	3.57	3.88	8.55

Analyzing the error between  $F_{lev3D}$  and  $F_{lev2D}$  shown in Table 4.6, it can be concluded that the levitation forces greatly differ from one another, especially with smaller depth values. Since the 2D simulations neglect magnetic flux dispersion in the 3D y-axis (which is the z-axis in the 2D simulations), as also considering that the magnetic field along the 3D y-axis is constant, it is to be expected that the levitation forces computed in the 2D simulations are higher than the ones computed in the 3D simulations. With this results, the 2D simulations made to estimate the optimal air gap are remade in the 3D environment.

### 4.6.3 Liquid Nitrogen and YBCO Container Weight for the Computation of the Total Weight

For the 3D simulations, the weight of the liquid nitrogen (LN2) and the container for the YBCO Bulk and the LN2 will be added to the analysis, since their weights cannot be neglected, especially the weight of the LN2. Figure 4.15 shows the volumes of the LN2 and the container, in blue and red, respectively. To determine the weight of the LN2 and the container, first their volumes need to be calculated.

Starting with the LN2 volume,  $V_{LN2}$ , first the volume of the rectangular prism  $V_{LN2}^{Box}$ , which is the total volume, that includes the YBCO and the outer volume below the YBCO, is calculated. Then, it is

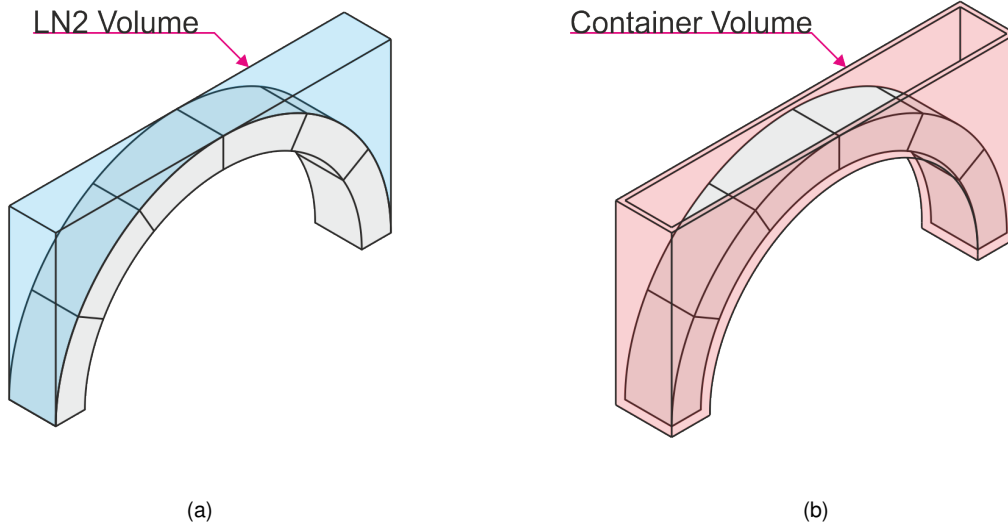


Figure 4.15: Representation of the volumes in the YBCO container: a) volume of Liquid Nitrogen; b) container volume.

subtracted from  $V_{LN2}^{Box}$  the volume of the halfdisk  $V_{HalfDisk}$ , which is the volume of the YBCO and the outer volume below the YBCO.  $V_{LN2}$  is then:

$$\begin{cases} V_{LN2}^{Box} = (2(R_{in} + T)) \cdot (R_{in} + T) \cdot D \\ V_{HalfDisk} = \frac{\pi}{2} (R_{in} + T)^2 D \\ V_{LN2} = V_{LN2}^{Box} - V_{HalfDisk} \end{cases} \quad (4.40)$$

Knowing the volume and knowing that the LN2 density is  $\rho_{LN2} = 0.807 \text{ gml}^{-1}$ , the LN2 weight  $F_g^{LN2}$  is:

$$\begin{cases} m_{LN2} = \rho_{LN2} V_{LN2} \\ F_g^{LN2} = m_{LN2} \cdot g \end{cases} \quad (4.41)$$

For the container, it encloses the YBCO bulk and the LN2 and it has a wall thickness  $T_{wall}$  on every dimension. The calculations are similar to the LN2: the total volume of the container box  $V_{Cont}^{Box}$  is calculated and it is subtracted from the total volume the outer volume  $V_{Outer}^{Box}$ , the LN2 Volume  $V_{LN2}$  and the YBCO Volume  $V_{YBCO}$

$$\begin{cases} V_{Cont}^{Box} = (2(T_{wall} + T + R_{in})) \cdot (2T_{wall} + T + R_{in}) \cdot (2T_{wall} + D) \\ V_{Outer}^{Box} = (2(T_{wall} + R_{in})) \cdot T_{wall} \cdot (2T_{wall} + D) + \frac{\pi}{2} (2(T_{wall} + R_{in}))^2 \\ V_{Cont} = V_{Cont}^{Box} - V_{Outer}^{Box} - V_{LN2} - V_{YBCO} \end{cases} \quad (4.42)$$

The material used for the calculation is the same one used for the YBCO car in Chapter 3, which as

a density of  $\rho_{Cont} = 0.171 \text{ gml}^{-1}$ , and so the weight of the container  $F_g^{Cont}$  is:

$$\begin{cases} m_{Cont} = \rho_{Cont} V_{Cont} \\ F_g^{Cont} = m_{Cont} \cdot g \end{cases} \quad (4.43)$$

With the weights of the container, the YBCO and the LN2, the total weight  $F_g^{Total}$  is:

$$F_g^{Total} = F_g^{Cont} + F_g^{YBCO} + F_g^{LN2}. \quad (4.44)$$

$F_g^{Total}$  will be used to calculate the net forces of the system in the 3D simulations of the following sections.

#### 4.6.4 3D FEM Simulations for the Computation of the Net Force Varying the YBCO Geometric Parameters

For this simulation, a parametric sweep is made regarding the geometric parameters air gap  $R_{air}$  and depth  $D$ . The values of the parametric sweep are shown in Table 4.7.

Table 4.7: Values of the geometric variables used for the computation of the YBCO levitation force  $F_{lev3D}$ .

Variables	Values [mm]
$R_{air}$	(5, 10, 15, 20, 25, 30, 35)
$T$	10
$D$	(16, 20, 24, 28, 32, 36, 40)
$d_{PM}$	0

For every air gap and depth, the weights of the YBCO, the LN2 and the container are calculated. The thickness of the wall of the containers was considered to be  $T_{wall} = 2.5 \text{ mm}$ , which is the minimum thickness possible for the material considered.

Figure 4.16 shows the values of the YBCO, LN2 and total weight,  $F_g^{YBCO}$ ,  $F_g^{LN2}$  and  $F_g^{Total}$ , respectively. Although the weight of the container is considered in the total weight, its influence is negligible in comparison to the weights of the YBCO bulk and the LN2, having a maximum value of 0.084 N, for an air gap of 35 mm and a depth of 40 mm.

Regarding the LN2 weight, for lower values of depth and air gap, the LN2 weight has a small value when compared to the weight of the YBCO. This means that for systems with a low value of depth and air gap the weight of the LN2 can be neglected. However, the weight of the LN2 increases quadratically with the air gap and linearly with the depth. This means that for higher values of air gap and depth, the weight of the LN2 can non longer be neglected. In fact, for an air gap of 35 mm, the increase in weight when considering the weight of the LN2 is of 13.4%, regarding the weight of the YBCO.

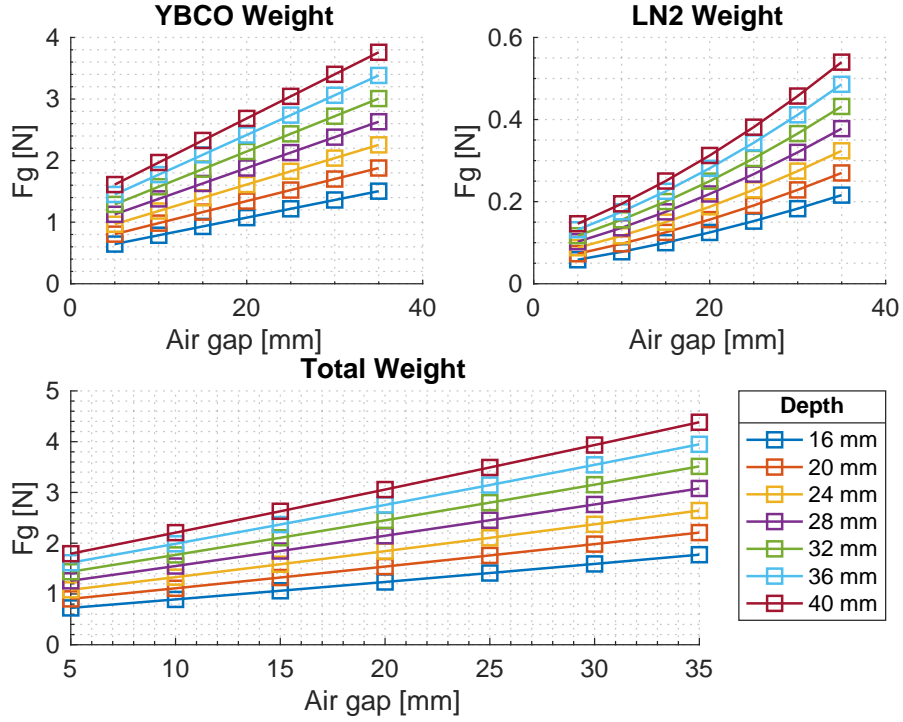


Figure 4.16: Weights of the YBCO, LN2 and the total weight for different air gaps and depths of the YBCO.

Having the total weight of the system and the YBCO Levitation Force computed, the net force  $F_{net}$  is calculated

$$F_{net} = F_{lev3D} - F_{YBCO}, \quad (4.45)$$

and the results of the computation of the levitation and the net force are shown in Figure 4.17.

In Figure 4.17, it can be seen that the net forces decrease with an increasing air gap and, between the air gap values of 30 to 35 mm, the net forces do not vary significantly with respect to the depth of the YBCO. This indicates that between those two values of air gap, the system has a net force close to zero, and the system is inherently stable, without needing additional weight. To see that the net forces are considerably small, Table 4.8 shows the values of the levitation and net force for the air gaps of 30 and 35 mm.

In Table 4.8 it can be seen that the net force stays constant with respect to the changes in depth, for air gap values of 35 mm. Analysing these information, it means that with air gap values above 35 mm, this system can not support its own weight, and the system would lose its radial symmetry.

With lower values of air gap, all the geometries are possible geometries, since additional load can be added to the system, in order to have a null net force.

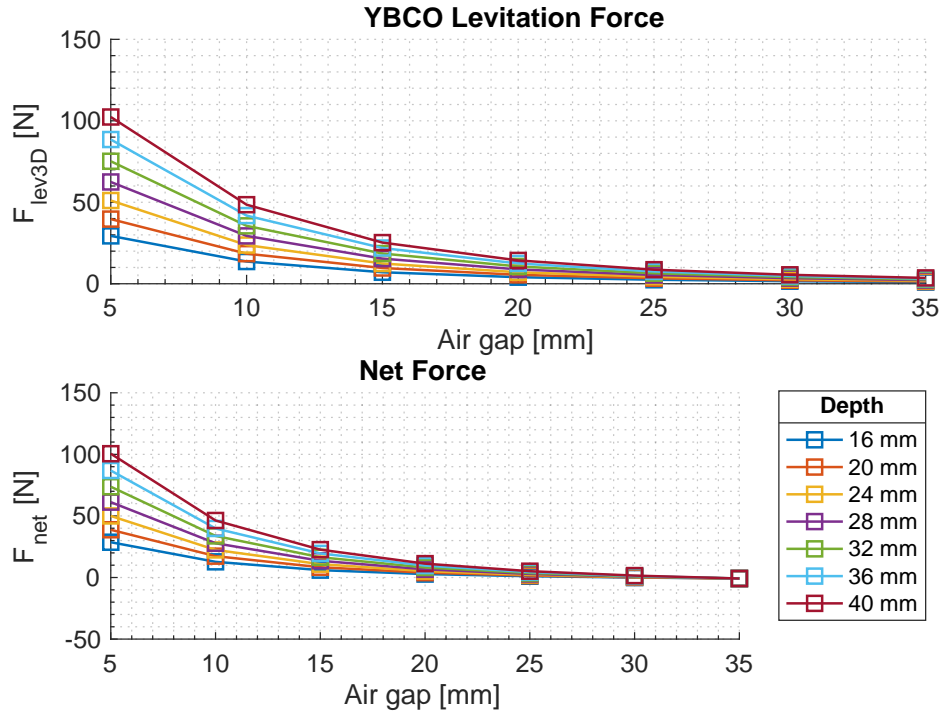


Figure 4.17: Net forces for a continuous magnetic track and for different air gaps and depths of the YBCO.

Table 4.8: Levitation and net force values for the air gap values of 30 and 35 mm.

Air gap [mm]	Depth [mm]	$F_{lev3D}$ [N]	$F_{net}$ [N]
30	16	1.56	-0.03
30	20	2.13	0.15
30	24	2.76	0.39
30	28	3.45	0.69
30	32	4.11	0.96
30	36	4.81	1.26
30	40	5.49	1.55
35	16	1.03	-0.75
35	20	1.40	-0.80
35	24	1.83	-0.82
35	28	2.25	-0.83
35	32	2.71	-0.80
35	36	3.15	-0.80
35	40	3.57	-0.81

#### 4.6.5 3D FEM Simulations for the Computation of the Net Force Varying the Permanent Magnets Spacing

This simulation is to determine the influence of the PM spacing  $d_{PM}$  regarding the levitation forces. In the simulations, the YBCO bulk is positioned on top of a PM, center aligned with it, as it is shown in Figure 4.18. The values of the parametric sweep are shown in Table 4.9. The levitation forces drop considerably with a magnetic track with spaced PM, and so, the air gap values considered for this simulation were only up to 20 mm, since the levitation forces of the simulations shown in Section 4.6.4

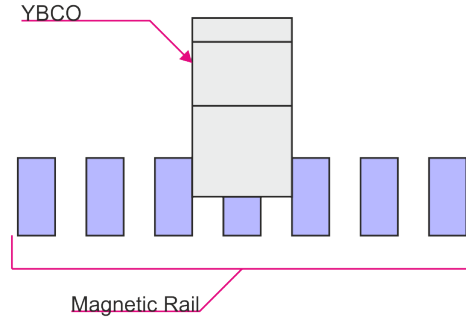


Figure 4.18: Depiction of the YBCO bulk centered with a PM of the magnetic track.

were close to zero for air gap values higher than 20 mm.

Table 4.9: Values of the geometric variables used for the computation of the YBCO levitation force  $F_{lev3D}$ .

Variables	Values [mm]
$R_{air}$	(5, 10, 15, 20)
$T$	10
$D$	(16, 20, 24, 28, 32, 36, 40)
$d_{PM}$	(10, 15)

The results of this simulation are shown in Figure 4.19. In Figure 4.19, it can be seen that the net forces are lower in comparison to the net forces of Figure 4.17. This is due to the fact that the levitation forces are lower in this situation, which results in a lower net force, since the weight of the system for each geometric configuration is the same as it is on the simulations of Section 4.6.4.

Comparing these results with the results of Section 4.6.4, it can be concluded that the possible YBCO geometric configurations reduce, given that the net force is positive until an air gap value of 20 mm. To see if there is a relationship between the levitation forces and the PM spacing, the relative difference between the levitation forces was made. The deviation from the levitation force of a PM spacing of 10 mm,  $Dev_{PM10}$  [%], and the deviation from the levitation force of a PM spacing of 15 mm,  $Dev_{PM15}$  [%], are described as

$$\begin{cases} Dev_{PM10} [\%] = \frac{|F_{lev} - F_{lev}^{PM10}|}{F_{lev}} \cdot 100 \\ Dev_{PM15} [\%] = \frac{|F_{lev} - F_{lev}^{PM15}|}{F_{lev}} \cdot 100 \end{cases} \quad (4.46)$$

where  $F_{lev}$  is the levitation force without PM spacing, and  $F_{lev}^{PM10}$  and  $F_{lev}^{PM15}$  are the levitation forces for a PM spacing of 10 and 15 mm, respectively. Figure 4.20 shows the results of the deviation in percentage of the levitation for the PM spacing of 10 mm and 15 mm.

Analyzing the deviations for both levitation forces with PM spacing, it can be seen that, as the depth of the YBCO increases, the value of the deviation for each air gap start to get similar. Also, for the air gap value of 20 mm, the deviations of the levitation forces remain almost constant, for different depths.

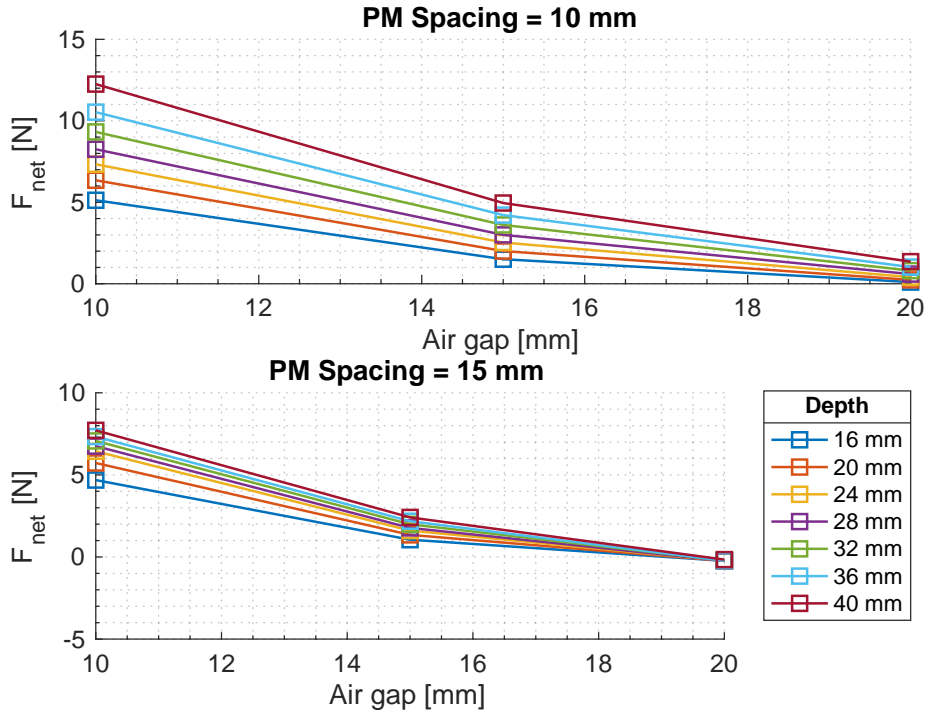


Figure 4.19: Net vertical forces for magnetic tracks with a PM spacing of 10 and 15 mm.

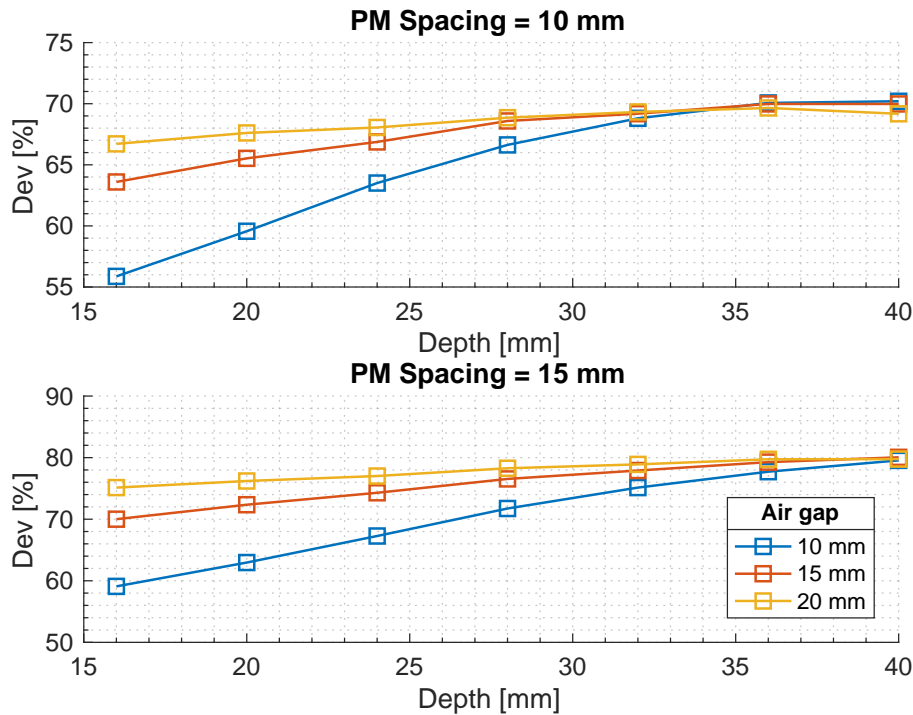


Figure 4.20: Levitation force deviations, in percentage, from the levitation forces of Section 4.6.4.

Regarding the computational and simulation aspect of the design of the new cylindrical geometry, the results shown in Figure 4.20 can provide us estimates for the levitation forces, without the need to make further simulations. With the results of Figure 4.17, if there is a need to interpolate the value of a levitation force for values of air gap, depth or PM spacing that were not simulated, the data shown in

Figure 4.20 proves to be rather useful, since it is a faster way to estimate the levitation forces and the FEM analysis is too time consuming, reaching from hours to days of simulation time.



## **Chapter 5**

# **Comparison of the Lateral Stability Between the Two Geometries**

This chapter presents a comparison for the lateral stability for the existing rectangular geometry and the new cylindrical geometry. The comparison will be made regarding the guidance forces of both geometries and their response to lateral perturbations.

## 5.1 Guidance Force of both geometries

Figure 5.1 shows the guidance forces measured of the rectangular geometry prototype, previously shown in Section 3.2.1, and the guidance force of the cylindrical geometry. The computations of the guidance forces for the cylindrical geometry were only made for the 2D FEM model, for a thickness of 10 mm and an air gap value of 35 mm. It was not possible to make the computation for the guidance forces on the 3D FEM model, since it is too time consuming, and it was not possible to have the results in time. However, considering the error between the levitation forces of the 2D and 3D Simulations (Table 4.6), the error for a depth of 40 mm is of 8.55 %, and so, it is assumed that the error for the guidance forces is of similar value and the main aspects of the analysis using the values of the 2D simulations are the same for the 3D FEM model.

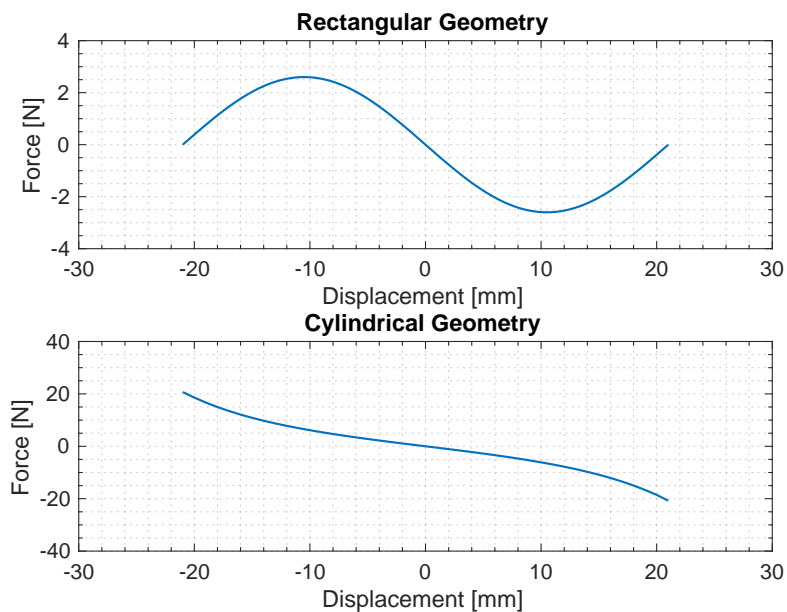


Figure 5.1: Lateral forces with respect to the lateral displacement of the rectangular and cylindrical geometries.

Analyzing the guidance force of both geometries shown in Figure 5.1, the cylindrical geometry presents a more linear force curve than the rectangular geometry. This indicates that the cylindrical geometry can be linearly controlled in the 21 mm displacement range, while in the rectangular geometry is not possible for the same displacement range.

Another difference between the two geometries is their range of motion. Although the maximum displacement for the rectangular geometry is of 21 mm, it is not due to a physical constraint, but because the system would be off centered from the magnetic track. In the Cylindrical Geometry, this does not happen, because the system cannot laterally displace more than its air gap value, since it will collide with the magnetic track. On top of that, as the Cylindrical YBCO gets closer to the magnetic track, the lateral forces increase in the opposite direction of the movement, which makes a stronger repulsive force in the YBCO.

## 5.2 Lateral Response of both geometries

In this section, it will be compared the lateral response of the rectangular and the cylindrical geometry. Since there is no information about the friction forces of the cylindrical geometry, the comparison of both geometries is made using the undamped response. This way, the comparison will focus on the differences of the guidance forces of the two geometries. The undamped responses of both geometries are also compared with a linear response of the same characteristics as the undamped responses, to analyze the linearity of the undamped responses.

### 5.2.1 Dynamic Equations and Comparison Model

For the rectangular geometry, the expression of the guidance force  $F_{\text{lat}}^{\text{Rect}}$  is (3.8), and it is shown here again, for easier readability:

$$F_{\text{lat}}^{\text{Rect}} = -2.6 \sin\left(\frac{\pi}{0.021}x\right). \quad (5.1)$$

For the cylindrical geometry, a cubic fit is made for the curve of the guidance force in Figure 5.1 and the guidance force  $F_{\text{lat}}^{\text{Cyl}}$  is:

$$F_{\text{lat}}^{\text{Cyl}} = -1.1 \cdot 10^6 x^3 - 3.8x^2 - 500x + 0.006. \quad (5.2)$$

With (5.1) and (5.2), the dynamic equations for the rectangular geometry and the cylindrical geometry are, respectively:

$$\begin{cases} m_{\text{Rect}}\ddot{x} + 2.6 \sin\left(\frac{\pi}{0.021}x\right) = 0 \\ m_{\text{Cyl}}\ddot{x} + (1.1 \cdot 10^6) x^3 + 3.8x^2 + 500x - 0.006 = 0 \end{cases}. \quad (5.3)$$

The solutions of (5.3) considered in the comparison are made for the initial conditions of  $x_0 = 20$  mm and  $\dot{x}_0 = 15$  mm/s. The solutions of the equations are to be compared with the response of a linear undamped system, which is

$$m\ddot{x} + kx = 0, \quad (5.4)$$

and its solution to a initial condition is

$$x = x_0 \cos\left(\sqrt{\frac{k}{m}}t\right). \quad (5.5)$$

Analyzing (5.5), and knowing that

$$\omega = \sqrt{\frac{k}{m}}, \quad (5.6)$$

a linear response of the same frequency as the solutions for both geometries can be made. This way, a comparison between the linear and non-linear response is made.

## 5.2.2 Results of the Comparison of the Dynamic Response of the Two Geometries

Figure 5.2 and Figure 5.3 show the solution of the dynamic equations to a initial condition of the rectangular geometry and the cylindrical geometry, as well as the linear response, for  $x_0 = 20$  mm and  $x_0 = 15$  mm, respectively.

Regarding the rectangular geometry, it is noticeable that the frequency of oscillation is different for each response. In the response for the initial condition of  $x_0 = 20$  mm, the frequency of oscillation is of 0.9 Hz, and for the response for the initial condition of  $x_0 = 15$  mm, the frequency is of 1.57 Hz, which is an increase of 70%. This is another indication that the system is non-linear, which makes it a more complex system to control, since the frequency of oscillations is not constant for different initial conditions.

For the cylindrical geometry, the frequency of oscillation does not vary much from the different initial conditions, being the frequency 6.85 Hz and 6.21 Hz for the initial conditions of  $x_0 = 20$  mm and  $x_0 = 15$  mm, respectively, which is a variation of about 10%. Also, the response of the system for both initial conditions is very similar to the linear response. This strongly indicates that the cylindrical geometry can be more easily controlled, since it can be modeled by a linear system.

Comparing the two systems, the cylindrical geometry has a more linear and steady response, for different initial conditions. Also, the cylindrical geometry is inherently more stable than the rectangular geometry, since the range of lateral motion is limited due to the geometric aspect of the design and, if the YBCO bulks get closer to the magnetic track, they are repelled with an higher force. In the rectangular geometry, this does not happen, since the distance of the YBCO bulks to the magnetic track is constant, regarding the lateral movement, and the force distribution as an entirely different pattern than the cylindrical geometry has.

Two possible disadvantages of the cylindrical geometry are that the frequency of oscillations is higher, which needs to be accounted for the control aspect of the system, and also if the YBCO bulk gets to close to the magnetic track, *flux pinning* can occur, and the YBCO remains trapped in that position, making the system off centered from the magnetic track. This two situations need to be present when designing the control system of the maglev.

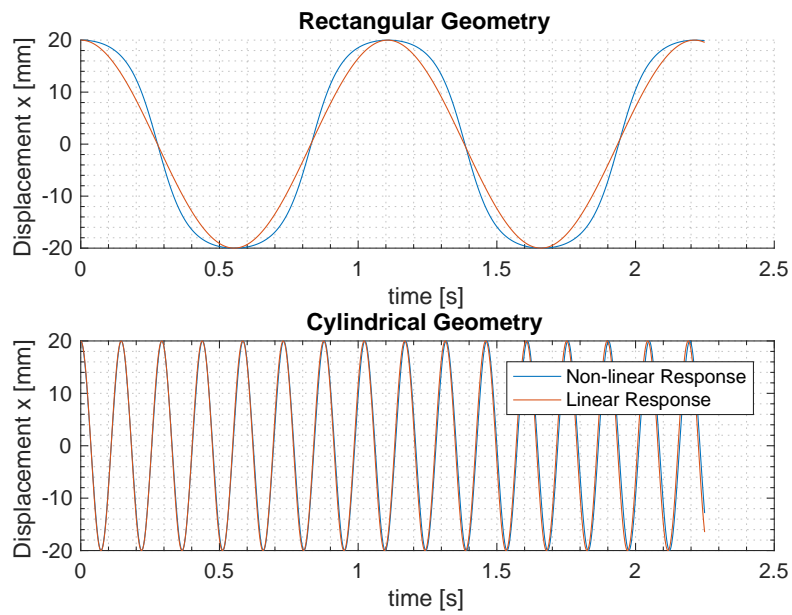


Figure 5.2: Undamped, Lateral response of the rectangular and cylindrical geometry for an initial displacement of  $x_0 = 20$  mm, as well as the linear response, for comparison.

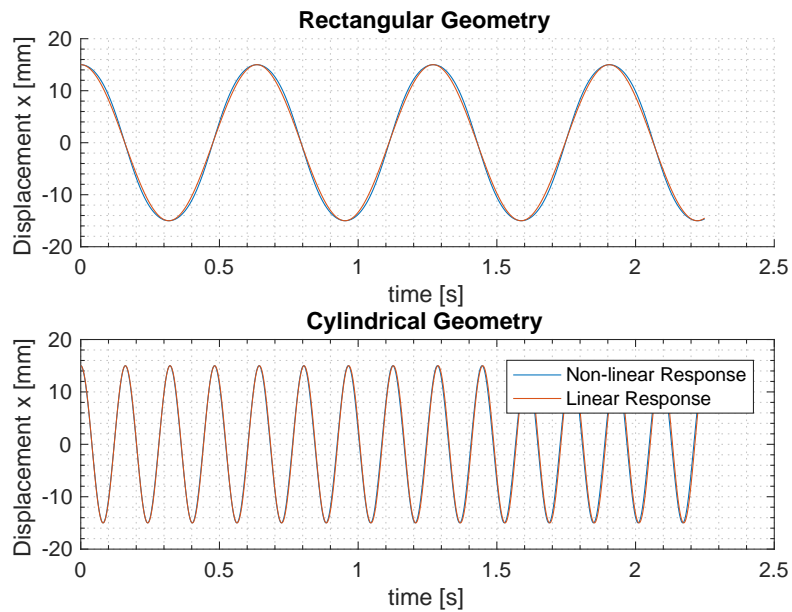


Figure 5.3: Undamped, Lateral response of the rectangular and cylindrical geometry for an initial displacement of  $x_0 = 15$  mm, as well as the linear response, for comparison.



## **Chapter 6**

# **Conclusions**

This chapter finalizes this work, summarizing conclusions and pointing out aspects to be developed in future work

## 6.1 Achievements

This dissertation consisted of a two part study: experimental study regarding an HTS maglev prototype, with a rectangular geometry; and the design and simulation of a new HTS maglev with a cylindrical geometry.

Regarding the rectangular geometry, first, experimental measurements were made regarding the lateral forces experienced by the YBCO. Second, the lateral response to initial conditions was recorded. Last, a model was developed to estimate the lateral response of the rectangular geometry. The model can estimate with a high degree of accuracy how the system behaves regarding lateral disturbances, which is essential for any type of control, being it an active or a passive type.

For the new cylindrical geometry, 2D and 3D simulations were made, to study the influence that the geometric parameters have on the levitation and guidance forces. These studies revealed a number of possible geometric configurations for which the system is vertically stable, i.e., it has a null net force, with the possibility to have load.

A study regarding the lateral forces of the cylindrical geometry was made, as well as a model for the response to lateral disturbances. This model was then compared to the model of the existing rectangular geometry. The main conclusions were that the cylindrical geometry is inherently more stable than the rectangular geometry, since it is a more linear system than the system of the rectangular geometry, and it has lateral movement limitations, due to the geometry, i.e, it is more difficult to derail than the system of the rectangular geometry. A disadvantage of the cylindrical geometry could be that, if the HTS are too close to the magnetic track, it can occur a *flux pinning* effect, making the HTS off centered.

## 6.2 Future Work

Simulations need to be made regarding the levitation and guidance forces in several positions of the magnetic track, since it is made of piecewise permanent magnets, and so, the levitation and guidance forces are not constant over the magnetic track.

An experimental prototype has to be developed, to validate the simulation results and also make experiments regarding the lateral response and stability of the system.

A study regarding the possibilities of flux pinning occurring in the HTS, when the YBCO bulks are closer to the magnetic track, and what are the influences in the lateral stability, linear and rotational movement of the maglev.

Finally, a study and development of a passive or active control system, to guarantee the lateral stability of the maglev needs to be in consideration, since the system was not studied regarding the stability when in movement.



# Bibliography

- [1] P. Branco and J. Dente. Design and experiment of a new maglev design using zero-field-cooled ybco superconductors. *IEEE Transactions on Industrial Electronics*, 59:1–1, 2011.
- [2] B. Painho. Protótipo laboratorial de um veículo de levitação magnética (maglev) com utilização de supercondutores. Master's thesis, Instituto Superior Técnico, Universidade de Lisboa, 2009.
- [3] J. McCurry, 2015. URL <https://www.theguardian.com/world/2015/apr/21/japans-maglev-train-notches-up-new-world-speed-record-in-test-run>. Accessed: 2018-05-05.
- [4] Linimo. URL <http://www.linimo.jp/en/index.php>. Accessed: 2018-05-05.
- [5] Wikipedia. URL [https://en.wikipedia.org/wiki/S1\\_line\\_\(Beijing\\_Subway\)](https://en.wikipedia.org/wiki/S1_line_(Beijing_Subway)). Accessed: 2018-05-10.
- [6] A. E. L. Luizar. Operação sincronizada dos motores lineares de tracção para um veículo de levitação magnética. Master's thesis, Universidade Federal do Rio de Janeiro, 2010.
- [7] S. H. F. d. Conceição. Balanço energético e armazenamento de energia do veículo de transporte urbano maglev-cobra. Master's thesis, Universidade Federal do Rio de Janeiro, 2014.
- [8] T. P. Sheahen. *Introduction to High-Temperature Superconductivity*. Plenum Press, 1<sup>st</sup> edition, 1994. ISBN:0-306-44793-2.
- [9] P. Ribeiro. "scale-up" of the portuguese superconductor type-zfc magnetic levitation system fulfilling the functional criteria of the maglev-cobra. Master's thesis, Instituto Superior Técnico, Universidade de Lisboa, 2015.
- [10] J. Arnaud. Use of superconductors in the excitation system of electric generators adapted to renewable energy sources. Master's thesis, Instituto Superior Técnico, Universidade de Lisboa, 2015.
- [11] H. Serieiro. Utilização de materiais supercondutores no circuito magnético de geradores eléctricos adaptados a fontes de energia renováveis. Master's thesis, Instituto Superior Técnico, Universidade de Lisboa, 2017.
- [12] F. S. Wells, A. Pan, X.-J. Wang, S. Fedoseev, and H. Hilgenkamp. Analysis of low-field isotropic vortex glass containing vortex groups in yba2cu3o72x thin films visualized by scanning squid microscopy. 5:8677, 03 2015.

- [13] C. Joong Kim. Suspension by flux pinning, 2009. URL <https://www.flickr.com/photos/51722970@N04/4757476544/>. Accessed: 2018-04-17.
- [14] A. Morandi. 2d electromagnetic modelling of superconductors. *Superconductor Science and Technology*, 25(10):104003, 2012. URL <http://stacks.iop.org/0953-2048/25/i=10/a=104003>.
- [15] A. J. Arsenio. Project of an inverse fuzzy model to compensate the oscillations of a superconducting planar levitation vehicle. Technical report, Instituto Superior Técnico, Universidade de Lisboa, 2016.
- [16] Z. Hong, A. Campbell, and T. Coombs. Computer modeling of magnetisation in high temperature bulk superconductors. *IEEE Transactions on Applied Superconductivity*, 17(2-3):3761 – 3764, 2007. doi: 10.1109/TASC.2007.899108.

# Appendix A

## Vector calculus

Some definitions and vector identities are listed in the section below.

### A.1 Vector identities

#### Distributive Properties

$$\nabla(\psi + \phi) = \nabla\psi + \nabla\phi \quad (\text{A.1})$$

$$\nabla \cdot (\mathbf{A} + \mathbf{B}) = \nabla \cdot \mathbf{A} + \nabla \cdot \mathbf{B} \quad (\text{A.2})$$

$$\nabla \times (\mathbf{A} + \mathbf{B}) = \nabla \times \mathbf{A} + \nabla \times \mathbf{B} \quad (\text{A.3})$$

#### Product of a scalar and a vector

$$\nabla \times (\rho\mathbf{A}) = \nabla\rho \times \mathbf{A} + \rho(\nabla \times \mathbf{A}) \quad (\text{A.4})$$

#### Vector dot Product

$$\frac{1}{2}\nabla(\mathbf{A} \cdot \mathbf{A}) = (\mathbf{A} \cdot \nabla)\mathbf{A} - (\nabla \times \mathbf{A}) \times \mathbf{A} \quad (\text{A.5})$$

#### Second Derivatives

$$\nabla \times (\nabla\phi) = 0 \quad (\text{A.6})$$

$$\nabla \cdot (\nabla \times \mathbf{u}) = 0 \quad (\text{A.7})$$


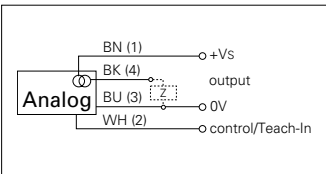

$$\nabla \times (\nabla \times \mathbf{A}) = \nabla(\nabla \cdot \mathbf{A}) - (\nabla \cdot \nabla)\mathbf{A} \quad (\text{A.8})$$



# Appendix B

## Technical Datasheets

### B.1 UNAM 12U9914/S14 Ultrasonic Distance Measuring Sensor

general data		photo
scanning range Sd	20 ... 200 mm	
scanning range close limit Sdc	20 ... 200 mm	
scanning range far limit Sde	20 ... 200 mm	
repeat accuracy	< 0,5 mm	
resolution	< 0,3 mm	
response time ton	< 30 ms	
release time toff	< 30 ms	
temperature drift	< 2 % of distance to target So	
sonic frequency	380 kHz	
adjustment	external Teach-in	
alignment aid	target indication flashing	
light indicator	yellow LED / red LED	
electrical data		connection diagram
voltage supply range +Vs	15 ... 30 VDC	
current consumption max. (no load)	35 mA	
output circuit	voltage output	
output signal	0 ... 10 V / 10 ... 0 V	
output current	< 20 mA	
residual ripple	< 10 % Vs	
short circuit protection	yes	
reverse polarity protection	yes	
mechanical data		 UL.eps • Analog voltage output 0 - 10 V
type	cylindrical threaded	
housing material	brass nickel plated	
width / diameter	12 mm	
height / length	70 mm	
connection types	connector M12	
ambient conditions		
operating temperature	-10 ... +60 °C	
protection class	IP 67	

### B.2 SCAIME K12 Force Sensor

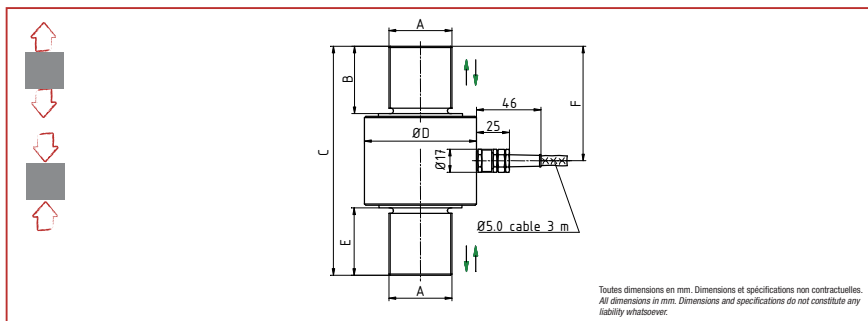
0 ... 0.5 kN à 0 ... 1 000 kN



- Construction en acier inoxydable
- Degré de protection IP67
- Faible encombrement
- Facilité de montage grâce aux 2 raccords mécaniques filetés
- *Stainless steel construction*
- *Protection level IP67*
- *Small dimensions*
- *Ease of assembly with the 2 thread mechanical joins*

Câblage - Wiring

+ alim.	+ signal	- signal	- alim.	Cran de calibration	Masse
+ excit.	+ signal	- signal	- excit.	Calibration control	Shield
marron	jaune	blanc	vert	gris	-
brown	yellow	white	green	grey	-



Charge Nominale (C.N.) kN	A	B	C	D	E	F
0.5, 1, 2, 5, 10	M12 x 1.75	24	79	50	20	37
20, 50	M20 x 1.5	25	90	59	25	45
100	M36 x 3	45	135	64	45	67.5
200	M45 x 3	50	170	79	50	85
500	M60 x 4	80	240	90	80	120
1 000	M100 x 3	110	300	130	110	150

0 ... 0.5 kN à 0 ... 1 000 kN

## Caractéristiques - Specifications

MÉCANIQUES	MECHANICAL		
Charge Nominale (C.N.)	Nominal load (C.N.)	0.5, 1, 5, 10 20, 50, 100, 200, 500, 1 000	kN
Force max. sans détérioration	Limit load	130	% C.N.
Force ultime avant rupture	Ultimate load	> 300	% C.N.
Déflexion sous force nominale	Position feedback at nominal load	< 0.1	mm
PRÉCISIONS	ACCURACY		
Erreur linéarité en traction ou compression	Linearity error for tension or compression	±0.1	% C.N.
Erreur combinée en traction et compression	Combined error for tension and compression	±0.4	% C.N.
Hystérésis	Hysteresis	±0.1	% C.N.
Répétabilité	Repeatability	±0.08	% C.N.
ÉLECTRIQUES	ELECTRICAL		
Impédance du pont	Bridge resistance	350	Ω
Résistance d'isolement	Insulation resistance	> 2 x 10 <sup>9</sup>	Ω
Tension d'alimentation	Supply voltage	2 ... 12	Vcc
Tension d'alimentation max.	Max. supply voltage	15	Vcc
Signal de sortie	Sensitivity	1.00	mV/V
GÉNÉRALES	GENERAL		
Dérive thermique du signal	Temperature coefficient of sensitivity	0.007	% C.N./°C
Dérive thermique de zéro	Temperature coefficient of zero signal	0.025	% C.N./°C
Plage de température compensée	Nominal temperature range compensated	-10 ... +70	°C
Plage de température opérationnelle	Service temperature range	-30 ... +80	°C
Degré de protection	Level of protection	IP67	
Matériau	Material	Acier Inoxydable Stainless steel	
Connexion	Connection	Câble 3 m	

## Options - Options

Cran de calibration	Calibration control	100	% C.N.
Plage de température compensée	Nominal temperature range compensated	(C.N. > 1 kN) -30 ... +100	°C
C.N. spéciales	Special ranges		

## Accessoires - Accessories



Rotules de charge EF  
Load adapters EF



CPJ



GM80 PA